

Universitätsmedizin Mannheim  
Medical Faculty Mannheim of Heidelberg University  
Master of Science in Biomedical Engineering

**Exploring Key Considerations and Challenges in  
Developing a Simulation Framework for Modeling  
Cardiac Electrophysiology and 12-Lead ECG  
Generation**

submitted by  
**Muhammed Saadeddin Koçak**  
supervised by  
**Prof. Dr. Jürgen Hesser**

September 2023



**Declaration:**

This thesis is the result of my independent investigation under supervision. Where my work is indebted to the work or ideas of others, for example from the literature or the internet, I have acknowledged this within the thesis.

I declare that this study has not already been accepted for any other degree, nor is it currently being submitted in candidature for any other degree.

I am aware that a false declaration could have legal implications.

.....



## Abstract

Cardiovascular diseases (CVDs) rank as the leading cause of mortality while 12-lead electrocardiogram (ECG) remains an elemental tool of clinical practice for diagnosis and surveillance of cardiac electrophysiology (CEP) abnormalities. Emerging data interpretation algorithms are increasingly emphasizing the need for ECG data in training and testing. However, the acquisition of clinical data is subject to specific limitations and strict regulations. At this juncture, *in silico* CEP modelling and 12-lead ECG simulations come to the rescue with their flexible and adequate infrastructure avoiding ethical constraints. Indeed, computational CEP field has been experiencing rapid growth, marked by continuous introduction of novel simulation environments.

The primary objective of this study is to explore key considerations and challenges in developing a simulation framework for modeling the electrical activity of a beating heart. Having this objective, we integrate a simulation pipeline generating 12-lead ECG signals. Moreover, the performance of the pipeline and setting changes are evaluated comparatively, facilitating potential distributions, activation time (AT) maps, and simulated ECG patterns.

The outcomes of this study portray the significance of contemplation points in ECG simulations. Namely, source models, mesh structures, region definitions, stimulus properties, and simulator options are found to be the key players in ECG generation. Furthermore, a simulation framework that is capable of generating 12-lead ECG signals is introduced. The setbacks of this framework caused by the limited availability of mesh structures and modeling parameters along with insights into future research and development directions are exhibited.



## Kurzfassung

Herz-Kreislauf-Erkrankungen sind die häufigste Todesursache, während das 12-Kanal-Elektrokardiogramm (ECG) in der klinischen Praxis für die Diagnose und Überwachung von Anomalien der kardialen Elektrophysiologie (CEP) nach wie vor ein grundlegendes Instrument darstellt. Neu entstehende Algorithmen zur Dateninterpretation betonen zunehmend den Bedarf an EKG-Daten für Training und Test. Die Erfassung klinischer Daten unterliegt jedoch bestimmten Einschränkungen und strengen Vorschriften. An diesem Punkt kommen die *in silico* CEP-Modellierung und 12-Kanal-EKG-Simulationen mit ihrer flexiblen und angemessenen Infrastruktur, die ethische Einschränkungen vermeidet, zur Rettung. Der Bereich der computergestützten CEP hat in der Tat ein schnelles Wachstum erfahren, das durch die kontinuierliche Einführung neuer Simulationsumgebungen gekennzeichnet ist.

Das Hauptziel dieser Studie ist es, die wichtigsten Überlegungen und Herausforderungen bei der Entwicklung eines Simulationsrahmens für die Modellierung der elektrischen Aktivität eines schlagenden Herzens zu untersuchen. Zu diesem Zweck integrieren wir eine Simulationspipeline, die 12-Kanal-EKG-Signale erzeugt. Darüber hinaus werden die Leistung der Pipeline und die Einstellungsänderungen vergleichend bewertet, um Potenzialverteilungen, Karten von Aktivierungszeit (AT) und simulierte EKG-Muster zu ermöglichen.

Die Ergebnisse dieser Studie verdeutlichen die Bedeutung von Betrachtungspunkten bei EKG-Simulationen. Es wurde nämlich festgestellt, dass das Quellenmodell, die Netzstruktur, die Regionsdefinitionen, die Stimuluseigenschaften und die Simulatoroptionen die wichtigsten Faktoren bei der EKG-Erzeugung sind. Darüber hinaus wird ein Simulationsrahmen vorgestellt, der in der Lage ist, 12-Kanal-EKG-Signale zu erzeugen. Die Nachteile dieses Rahmens, die durch die begrenzte Verfügbarkeit von Netzstrukturen und Modellierungsparametern verursacht werden, sowie Einblicke in zukünftige Forschungs- und Entwicklungsrichtungen werden aufgezeigt.



## **Acknowledgements**

I would like to express my sincere gratitude to my advisor Prof. Dr. Jürgen Hesser for individual support and encouragement throughout my studies. Their invaluable insights, motivation, and enthusiasm have been instrumental in shaping my studies and personal growth.

Besides, I must express my gratitude to Valentin Schmid and Marcus Buchwald whose ideas contributed significantly to my thesis.

Lastly, I want to extend my heartfelt gratitude to my family. Their unwavering support has been essential throughout my studies and life.



# Contents

## List of Figures

## List of Tables

## Acronyms

<b>1</b>	<b>Introduction</b>	<b>1</b>
<b>2</b>	<b>Background</b>	<b>3</b>
2.1	Cardiac Electrophysiology . . . . .	3
2.1.1	Cellular Electrophysiology of the Heart . . . . .	3
2.1.2	Activation of the Heart . . . . .	4
2.1.3	Conduction System of the Heart . . . . .	5
2.2	Model Development . . . . .	6
2.2.1	Motivation . . . . .	7
2.2.2	Source Description . . . . .	7
2.2.3	Forward Problem . . . . .	10
2.3	Electrocardiogram . . . . .	11
<b>3</b>	<b>Related Work</b>	<b>16</b>
3.1	Modeling for ECG Interpretation . . . . .	16
3.1.1	Healthy Heart Modelling . . . . .	17
3.1.2	Abnormal Heart Modelling . . . . .	17
3.2	openCARP . . . . .	18
<b>4</b>	<b>Materials and Methods</b>	<b>20</b>
4.1	Source Model . . . . .	20
4.2	Meshes . . . . .	21
4.3	Regions . . . . .	22
4.3.1	Ionic Model . . . . .	22
4.3.2	Conductivities . . . . .	23
4.3.3	Bath . . . . .	24
4.4	Stimuli . . . . .	24
4.4.1	Stimulus Type . . . . .	25

4.4.2	Stimulus Location . . . . .	25
4.5	Leads . . . . .	25
4.5.1	Lead Identification . . . . .	25
4.5.2	ECG Calculation . . . . .	25
4.6	Simulator Options . . . . .	26
4.7	Visualization . . . . .	26
4.8	Writing . . . . .	27
<b>5</b>	<b>Results</b>	<b>30</b>
5.1	Sample Run . . . . .	30
5.2	Source Model . . . . .	32
5.3	Resampling . . . . .	33
5.4	Mesh . . . . .	34
5.5	Ionic Model . . . . .	35
5.6	Conductivity Factor . . . . .	35
5.7	Bath Conductivity . . . . .	35
5.8	Stimulus Location . . . . .	35
5.9	Time Step . . . . .	36
<b>6</b>	<b>Discussion</b>	<b>60</b>
<b>7</b>	<b>Conclusion</b>	<b>63</b>
<b>8</b>	<b>Bibliography</b>	<b>64</b>
<b>A</b>	<b>Appendix</b>	<b>74</b>
A.1	Supplementary ECG Measurements . . . . .	74

# List of Figures

2.1	Phases of a prototypical ventricular AP and underlying currents[8] . . . . .	4
2.2	Conduction system of the heart[14] . . . . .	6
2.3	Torso with multiple regions of differing isotropic conductivity[41] . . . . .	11
2.4	Peaks of a typical ECG waveform on Lead II[8] . . . . .	12
2.5	Standard lead positions[14] . . . . .	14
2.6	Characteristic APs drawn for different cardiac structures[8] . . . . .	15
4.1	Locations of the most sensitive stimuli reported by Cranford et al.[63]	28
4.2	Locations of the leads[90] . . . . .	29
5.1	Extracellular potentials of the torso in the sample run . . . . .	31
5.2	Extracellular potentials of the heart in the sample run . . . . .	32
5.3	Transmembrane potentials of three different points on the epicardial surface in the sample run. Three points are chosen from the apex, LV freewall, and base of the heart. . . . .	33
5.4	Limb leads ECG measurements of the sample run . . . . .	37
5.5	Chest leads ECG measurements of the sample run . . . . .	38
5.6	AT map of the sample run. Nodes are assigned with time instants corresponding to the moment they cross the threshold potential. . . . .	39
5.7	Transmembrane potentials of the heart simulated with different source models . . . . .	39
5.8	Extracellular potentials of the torso simulated with meshes having different resampling rates . . . . .	40
5.9	Limb leads ECG measurements of meshes with different resampling rates. Purple line is for the mesh resampled to a target mean edge length of 3,000 $\mu m$ and green line is for the mesh resampled to a target mean edge length of 5,000 $\mu m$ . . . . .	41
5.10	Chest leads ECG measurements of meshes with different resampling rates. Purple line is for the mesh resampled to a target mean edge length of 3,000 $\mu m$ and green line is for the mesh resampled to a target mean edge length of 5,000 $\mu m$ . . . . .	42
5.11	Extracellular potentials of the torso simulated with different mesh structures . . . . .	43

5.12	Extracellular potentials of the heart simulated with different ionic models . . . . .	44
5.13	Limb leads ECG measurements of meshes with different ionic models. Purple line is for the simulation with the Courtemanche ionic model and green line is for the simulation with the tenTusscherPanfilov ionic model. . . . .	45
5.14	Chest leads ECG measurements of meshes with different ionic models. Purple line is for the simulation with the Courtemanche ionic model and green line is for the simulation with the tenTusscherPanfilov ionic model. . . . .	46
5.15	Extracellular potentials of the heart simulated with different conductivity factors . . . . .	47
5.16	AT maps of the heart simulated with different conductivity factors . . . . .	48
5.17	Limb leads ECG measurements of meshes with different conductivity factors. Purple line is for the simulation with conductivity factor of 7 and green line is for the simulation with conductivity factor of 8 . . . . .	49
5.18	Chest leads ECG measurements of meshes with different conductivity factors. Purple line is for the simulation with conductivity factor of 7 and green line is for the simulation with conductivity factor of 8 . . . . .	50
5.19	Extracellular potentials of the heart simulated with different bath conductivities . . . . .	51
5.20	Extracellular potentials of the torso simulated with different bath conductivities . . . . .	52
5.21	Extracellular potentials of the heart simulated from different stimulation points . . . . .	53
5.22	Extracellular potentials of the torso simulated from different stimulation points . . . . .	54
5.23	AT maps of the heart simulated from different stimulation points . . . . .	55
5.24	Limb leads ECG measurements of meshes with different stimulation points. Purple line is for the simulations stimulated from the left ventricle and green line is for the simulations stimulated from the right ventricle. . . . .	56
5.25	Chest leads ECG measurements of meshes with different stimulation points. Purple line is for the simulations stimulated from the left ventricle and green line is for the simulations stimulated from the right ventricle. . . . .	57
5.26	Limb leads ECG measurements of meshes with different time steps. Purple line is for the simulations run with a time step of $400 \mu s$ and green line is for the simulations run with a time step of $100 \mu s$ . . . . .	58
5.27	Chest leads ECG measurements of meshes with different time steps. Purple line is for the simulations run with a time step of $400 \mu s$ and green line is for the simulations run with a time step of $100 \mu s$ . . . . .	59

A.1	Limb leads ECG measurements of different mesh structures. Purple line is for Torso 1 and green line is for Torso 2 . . . . .	75
A.2	Chest leads ECG measurements of different mesh structures. Purple line is for Torso 1 and green line is for Torso 2 . . . . .	76
A.3	Limb leads ECG measurements of meshes with different bath conductivities. Purple line is for the simulations with a bath conductivity of 0.7 and green line is for the simulations with a bath conductivity of 1. . . . .	77
A.4	Chest leads ECG measurements of meshes with different bath conductivities. Purple line is for the simulations with a bath conductivity of 0.7 and green line is for the simulations with a bath conductivity of 1. . . . .	78

# List of Tables

5.1	Computation durations for the simulation of one heart cycle in different source models . . . . .	33
5.2	Mesh properties and computation durations for the simulation of one heart cycle in meshes resampled to different target mean edge lengths	34
5.3	Correlation coefficients for various simulation settings . . . . .	34

# Acronyms

**AP** action potential.

**AT** activation time.

**AV** atrioventricular.

**BEM** boundary element methods.

**BSP** body surface potential.

**CEP** cardiac electrophysiology.

**CV** conduction velocity.

**CVD** cardiovascular diseases.

**ECG** electrocardiogram.

**LA** left arm.

**LL** left leg.

**LV** left ventricle.

**MRI** magnetic resonance imaging.

**ODE** ordinary differential equation.

**PDE** partial differential equation.

**PMJ** Purkinje-myocardial junction.

**RA** right arm.

**RV** right ventricle.

**SA** sinoatrial.

# 1 | Introduction

Worldwide, cardiovascular diseases (CVDs) stand as the primary cause of death, claiming approximately 17.9 million lives each year. CVDs encompass a cluster of disorders affecting the heart and blood vessels, which includes conditions like coronary heart disease, cerebrovascular disease, rheumatic heart disease, and other related ailments. Heart attacks and strokes collectively account for more than four out of five CVD-related deaths. Tragically, a significant portion of these deaths, around one-third, occur prematurely among individuals under the age of 70. Spotting these individuals most vulnerable to CVDs and guaranteeing they get the right treatment can stop early deaths[1].

Arrhythmias, myocardial infarction, and ischemia rank among the most critical CVDs that are subject to diagnosis through interpretation of cardiac electrical activity[2, 3, 4]. Effective monitoring of this activity enables medical practitioners to establish a framework for spotting individuals with increased risk. At this point, 12-lead electrocardiogram (ECG) upholds a pivotal position in assessing the risk associated with electrophysiological irregularities of the heart.

The word ECG originates from the German language "elektro-kardiographie" and portrays the non-invasive capture of the heart's electrical activity from the body surface. It was pioneered by Dutch physician Einthoven back in 1902 earning him the Nobel Prize in 1924[5, 6]. The utilization of the ECG has rapidly evolved beyond basic heart rate monitoring to the interpretation of intricate arrhythmias, myocardial infarction, and various other ECG irregularities[7]. Further on, ECG is expanding as an integral part of various clinical and experimental modalities. One such example is ECG imaging where ECG information is combined with anatomical information for non-invasive endo-, epi-, or trans- membrane potential mapping[8].

Paradoxically, as the use of ECG becomes more widespread, the demand for patient-specific data also intensifies. Consequently, computational models in cardiology have gained significantly greater value than in the past[9]. While these computational models may refer to many physiologic aspects of the heart, we will mainly focus on cardiac electrophysiology (CEP). At this juncture, *in silico* CEP models offer the unique capability to investigate CEP with a degree of quantitative precision and biophysical intricacy that exceeds current possibilities within other research methods[10].

In this study, we aim to realize a simulator framework for generating ECG signals using the openCARP tool. By this, we demonstrate challenges and considerations in

the development of a framework for CEP modeling. Specifically, through simulations of ECG signals originating from a beating heart, deliberations on such a task are investigated in detail. Simulation results are evaluated in terms of compatibility with the current literature and assessed how compliant they are with clinical data.

The thesis is structured as follows:

- Chapter 2 provides brief background information about cardiac electrophysiology, CEP model development, and ECG.
- Chapter 3 outlines the most recent literature relating to modeling for ECG interpretation. Also, similar studies to this thesis that utilize the openCARP framework are exhibited.
- In Chapter 4, the pipeline construction steps are presented along with an overview of the road map that was followed. Details regarding the materials and methods that were employed are given with justifications of the rationale.
- In Chapter 5, the simulation outcomes are presented in a comparative way.
- Chapter 6 discusses the results and gives insights into considerations and challenges in the development of a framework for ECG simulations. Moreover, further directions are anticipated within this chapter.
- In Chapter 7, we conclude the study by summarizing the findings of this study.

## 2 | Background

In this section, the essential background information that lays the foundation for comprehending the materials and methods employed in this study is presented.

### 2.1 Cardiac Electrophysiology

CEP studies followed a deductive methodology rather than an inductive one meaning it was not the discovery of cell-level behavior of the heart that initiated the understanding of the heart, but it was the discovery of ECG by Einthoven[11]. Although the history occurred in such a way, we explore the electrical and physiological dynamics of the heart, starting from cellular-level and extending to organ-level.

#### 2.1.1 Cellular Electrophysiology of the Heart

Cell-level electrophysiology studies date back to 1949 when Ling and Gerard conducted research on cell membrane potentials in muscle fibers of the frog sartorius, engaging microelectrodes[12]. Following, studies similar to the one conducted by Nether et al. deepened our interpretation of micro-level behavior of organs, later leading to a more sophisticated understanding of the heart's cellular architecture[13].

The smallest functional units of the heart are called myocytes or cardiomyocytes[14]. Each myocyte is surrounded by a lipid bilayer known as sarcolemma. Importantly, this bilayer exhibits a very high dielectric constant since it is impermeable to ions. Ions are only allowed to cross the membrane through special protein structures, namely ion channels[8]. Resulting from such structure and more, excitability stands as one of the cornerstone attributes of myocytes. A small stimulus can induce a way stronger reaction, action potential (AP). This enables the succession of excitation in nearby tissue resulting in seamless propagation of electrical signals[15].

The complex structure and functionality of myocytes are yet to be discovered and a comprehensive elaboration of the present knowledge extends far beyond the scope of this study. The interested reader is kindly referred to more medical literature on this issue[16]. Instead, the tissue structure of the heart and its relation with the organ-level behavior will be delineated.

The heart muscle consists of five distinct types, each characterized by its anatomy and function. The sinoatrial (SA) node, atrioventricular (AV) node, His-Purkinje system, atrial muscle, and ventricular muscle. In a normal physiological state, the

initiation of the cardiac impulse is predominantly orchestrated by the SA node, which functions as the heart's natural pacemaker despite the AV node and His-Purkinje system having the capacity of pacemaking. However, the AV node and the His-Purkinje system play mainly a critical role in conduction, ensuring the synchronized transmission of the cardiac impulse across the myocardium. Meanwhile, the atrial and ventricular muscles engage in force generation as APs traverse through them[8]. Proper propagation of impulses is only possible through a specialization of the cardiac tissue as described.

### 2.1.2 Activation of the Heart

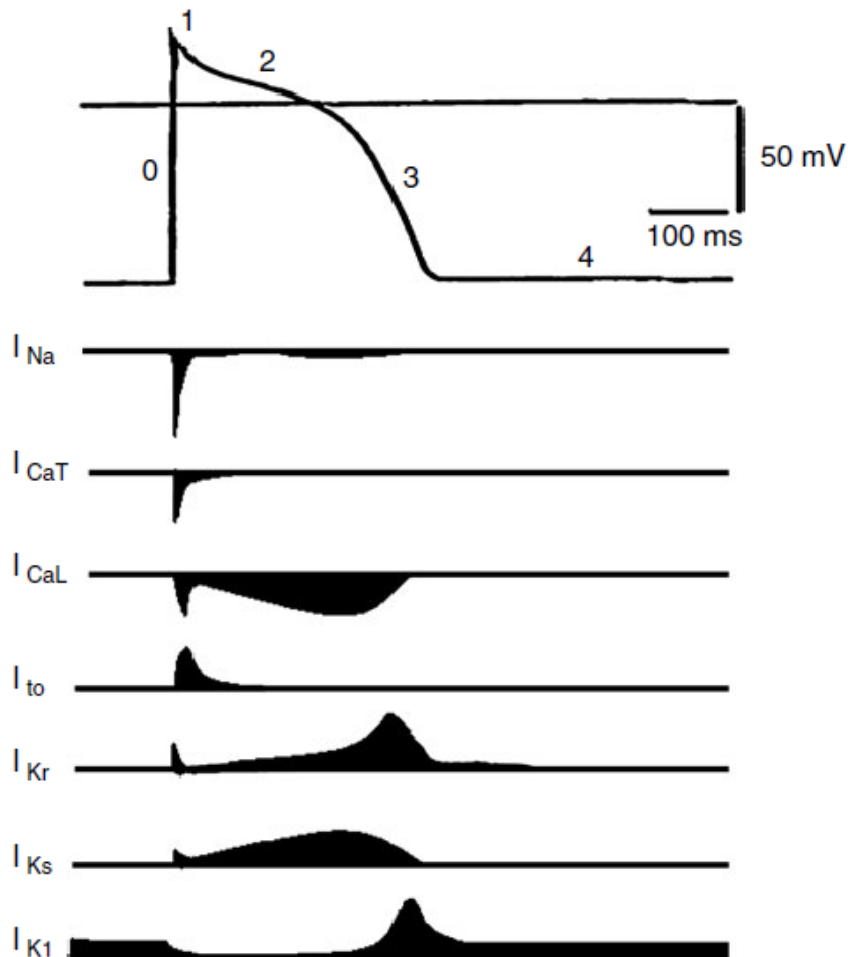


Figure 2.1: Phases of a prototypical ventricular AP and underlying currents[8]

Hodgkin and Huxley conducted the pioneering study in 1952 justifying the transmembrane potential changes in the nerve fiber[17]. Further on, this discovery enabled the capture of the complex nature of organ-level and thereby system-level

function of human physiology. Likewise, establishing a connection between the micro-level behavior of the heart and its macro-level dynamics of it demands a distinct understanding of APs.

The AP fundamentally constitutes an electrical transient reversal of membrane potential capable of propagating over considerable distances while maintaining its amplitude. Once initiated, these processes operate autonomously, dissociating from the initiating stimulus. To trigger AP, the stimulus must overcome a specific level named threshold in terms of amplitude and duration[15]. In cardiac tissue, AP has a distinctive contour shown in Fig. 2.1 with several phases detailed below.

- Phase 0 is the depolarization phase that occurs when the excitation threshold is exceeded. The inward current of  $Na$  ions increases the membrane voltage steeply. This phase also triggers the  $K$  currents which contribute to the termination of this phase and immediate repolarization after.
- Phase 1 is the early repolarization phase which corresponds to the moment  $Na$  ion channels are getting closed.
- Phase 2 is referred to as the plateau phase where the inflow of  $Ca$  ions is balanced with the outflow of  $K$  ions. Nearly a constant transmembrane voltage is maintained during this phase.
- Phase 3 is the repolarization phase. Here,  $Ca$  ion channels are closed, and the outward current of  $K$  ions results in a decrease in potential difference.
- Phase 4 is the resting phase. In this phase, the heart remains in resting potential and diastole state.

### 2.1.3 Conduction System of the Heart

Having explored the activation of the heart tissue, our focus shifts to the propagation of the AP within the broader organizational structure of the heart at organ-level. Comprehending the heart's conduction system is crucial for grasping the underlying principles of signal propagation throughout the entire body. Therefore, it is given in Fig. 2.2.

The cardiac electrical activity originates from the SA node and swiftly traverses through the atria. The electrical isolation between the atria and ventricles prevents chaotic transmission of AP to the lower part of the heart. Electrical signals converge at the AV node and an essential delay to the transmission is introduced allowing complete ejection of the blood from the atria. It must be stressed the paramount significance of the AV node's proper operation since it is a common cause of cardiac pathologies[18].

The network of the heart's ventricles assumes a leading role in harmonized contractions. These contractions are essential for effectively propelling blood into the circulatory system while maintaining the required pressure levels. In particular,

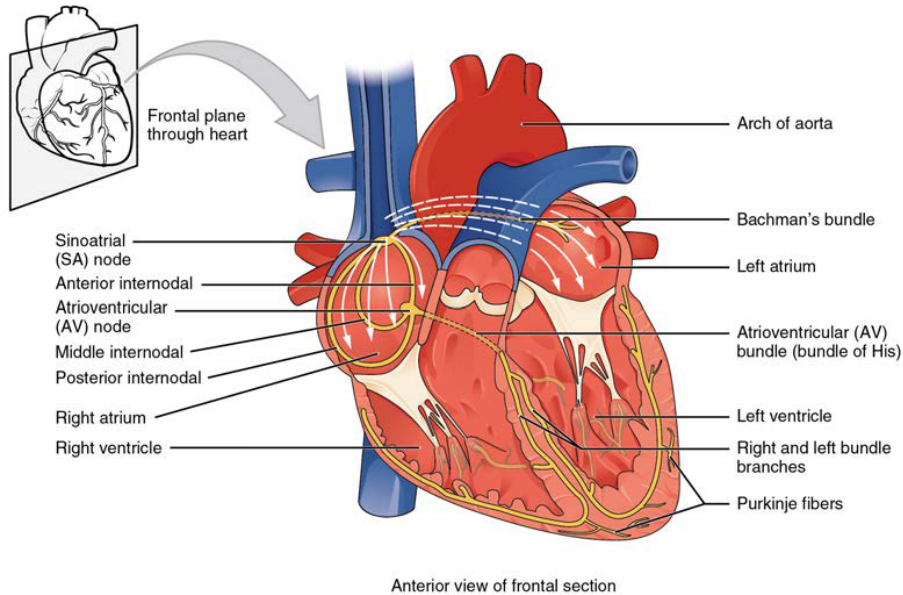


Figure 2.2: Conduction system of the heart[14]

ventricular contraction follows a pattern initiating from the heart's apex and radiating towards the base. This orderly propagation is realized thanks to the special conduction system comprising the bundle of His, bundle branches, and Purkinje fibers[14].

The bundle of His functions as a conduit, dividing into left and right branches. Further ramifying, Purkinje fibers empower fast and orderly propagation of electrical impulses from apex to base, consequently contracting the heart from bottom to up. Such coordinated contraction pushes the blood into the lungs through the pulmonary veins and into the circulatory system through the aorta.

## 2.2 Model Development

The collective electrical activity of the individual myocytes is reflected on the surrounding tissue as potential differences. As the stimulus travels through the cardiac tissue, its propagation is influenced by the surrounding environment, leading to the attenuation of the signals. This phenomenon results in distinct voltage patterns that are observed on the body surface. The calculation of body surface potentials (BSPs) originating from the cardiac activity is named as the forward problem of ECG. However, before diving into the specifics of this problem, it is necessary to cover how to model the CEP with appropriate source descriptions. Later, we must contemplate how to map the local cardiac activity to the torso surface while accounting for specific human anatomy. In this section, it is attempted to illustrate both from the perspective of today's literature. However, more importantly, the motivation behind the cardiac model development is discussed.

### 2.2.1 Motivation

- Computational models provide a common framework that is exceptionally capable of bringing diverse experimental and clinical data together without the burden of ethical constraints[10, 9].
- These models are rooted in physiology and physics instead of statistics. Conducting computer simulations based on these can uncover hidden diagnostic information and forecast how treatments will work for individual patients[9].
- A feedback mechanism is introduced that is involving computational models for patient specific medicine. Namely, available patient data can be fed into the personalized model with physiologic constraints intrinsically applied and this model can guide diagnostics, prognostics, or therapy. After the intervention, new data collected from the patient can again be fed into the algorithm for further needs or a model development.
- Computer simulations can be run on an altered model representing a cardiac disorder. These simulations resulting in immense amounts of data can be utilized for the training of emerging data-driven and machine learning-based algorithms.
- The impact of drugs or diseases can be introduced to the cardiac model giving prospective analysis of interventions without performing ethically challenging experiments on animals or humans[9].

### 2.2.2 Source Description

#### Bidomain Model

The bidomain model relates intracellular potential,  $\Phi_i$ , to extracellular potential,  $\Phi_e$  through the transmembrane current density,  $I_m$ [19, 20]. The relation is formulated as:

$$\nabla \cdot \sigma_i \nabla \Phi_i = \beta I_m - I_i \quad (2.1)$$

$$\nabla \cdot \sigma_e \nabla \Phi_e = \beta I_m - I_e \quad (2.2)$$

where  $\sigma_i$  and  $\sigma_e$  are intracellular and extracellular conductivities.  $\beta$  refers to the bidomain surface-to-volume ratio, whereas  $I_i$  and  $I_e$  are intracellular and extracellular current density stimuli. Transmembrane current is given by:

$$V_m = \Phi_i - \Phi_e \quad (2.3)$$

$$I_m = C_m \frac{\partial V_m}{\partial t} + I_{ion} - I_{tr} \quad (2.4)$$

$$\frac{\partial \eta}{\partial t} = f(V_m, \eta, t) \quad (2.5)$$

$$I_{ion} = g(V_m, \eta, t) \quad (2.6)$$

where  $I_{tr}$  is transmembrane current density stimulus, as delivered by an intracellular electrode,  $C_m$  is the membrane capacitance per unit area,  $V_m$  is the transmembrane voltage, and  $I_{ion}$  is the current density flowing through the ionic channels. Homogeneous Neumann boundary conditions are imposed at the boundaries of the myocardial tissue and the torso. They are formulated as:

$$\sigma_i \nabla \Phi_i \cdot \vec{n} = 0 \quad (2.7)$$

$$\sigma_e \nabla \Phi_e \cdot \vec{n} = 0 \quad (2.8)$$

where  $\vec{n}$  is the vector normal to the boundary. When heart tissue is surrounded by a bath with conductivity  $\sigma_b$  and potential  $\Phi_b$  following are satisfied at the bath tissue interface:

$$\Phi_e = \Phi_b \quad (2.9)$$

$$\sigma_e \nabla \Phi_e \cdot \vec{n} = \sigma_b \nabla \Phi_b \cdot \vec{n} \quad (2.10)$$

Since  $V_m$  are contingent on  $I_m$ , the equations at the tissue-level are interconnected with those at the cellular-level. Consequently, the entire model comprises a system of two partial differential equations (PDEs) along with a specific count of ordinary differential equations (ODEs). These equations are notably difficult to solve due to their strong non-linear nature[21]. In other words, the bidomain equations so far are referred as the parabolic-parabolic form. Using the definition of  $V_m$  into the Eq. 2.1 and Eq. 2.2, we can form:

$$\nabla(\sigma_i + \sigma_e) \nabla \Phi_e = -\nabla \cdot \sigma_i \nabla V_m - I_e - I_i \quad (2.11)$$

$$\nabla \cdot \sigma_i \nabla V_m = -\nabla \cdot \sigma_i \nabla \Phi_e + \beta I_m \quad (2.12)$$

Here, Eq. 2.11 is an elliptic and Eq. 2.12 is a parabolic equation. This form is referred as elliptic-parabolic and it is more convenient for tissue scale simulations.

For the solvers of the above bidomain equations reader is kindly referred to the study of Vigmond et al.[22]. Despite the complexity and demand for high resolution mesh structures for robust solution of the bidomain equations, this model remains to be the most accurate cardiac source model in current literature[23].

## Monodomain Model

Immediately after the commonly used bidomain model, another frequently used model, monodomain model, emerges[24]. Essentially, it is a simplification of the bidomain model through the assumption of proportional conductivity tensor between intracellular and extracellular spaces[20, 21]. Assuming a monodomain conductivity tensor,  $\sigma_m$ , defined as the half of the harmonic mean of intracellular and extracellular conductivities:

$$\sigma_m = \frac{\sigma_i \sigma_e}{\sigma_i + \text{sigma}_e} \quad (2.13)$$

Eq. 2.11 and Eq. 2.12 are reduced to:

$$\beta C_m \frac{\partial V_m}{\partial t} = \nabla \cdot (\sigma_m \nabla V_m) - \beta (I_{ion}(V_m, \eta) - I_{tr}) \quad (2.14)$$

Although the assumption of equal anisotropy does not hold in physiological sense, monodomain model still offers a close approximation for transmembrane potential propagation[25]. The volume conductor cannot influence the transmembrane voltage distribution in this approach since it is assumed that cardiac electric sources are immersed in an unbounded conductive medium. Therefore, this model is not recommended for calculation of BSP mapping with many points on the torso surface[26, 23].

### Pseudobidomain Model

A pseudobidomain formulation combines the computational advantages of monodomain approach with a fullblown bidomain. Electrical activity of the cardiac tissue is computed using the Eq. 2.14 whereas  $\Phi_e$  distributions are computed through solving:

$$-\nabla \cdot (\sigma_i + \sigma_e) \nabla \Phi_e = \nabla \cdot \nabla V_m \quad (2.15)$$

and

$$-\nabla \cdot \sigma_b \nabla \Phi_e = 0 \quad (2.16)$$

In this formulation, membrane potential is computed at a time step governed by the ODE system while extracellular potentials are computed at a desired granularity, typically way less frequent. Compared to the recovery techniques from the monodomain model, pseudobidomain model provides a faithful interaction with the bath[26]. Application of this model on ventricles provided accurate simulations with a computational performance seven times faster than the bidomain model[27].

### Eikonal Model

Unlike direct membrane potential calculations, Eikonal model is based on macroscopic kinetics of the wavefront propagation[20]. Defining activation times (ATs) as  $T$  for each node  $x$ , Eikonal equations take the form:

$$\sqrt{\nabla T(x)^\top M \nabla T(x)} = 1 \quad (2.17)$$

$$T(x) = T_0 \quad \text{for} \quad x \in \Gamma \quad (2.18)$$

where  $M$  is the squared conduction velocity (CV) tensor,  $T_0$  is the initial conditions for the activation sites  $\Gamma$ . Transmembrane potentials are inferred from the ATs:

$$V_m(x, t) = U(x, t - T(x)) \quad (2.19)$$

where  $U$  is an AP time course[28].

Solutions for these equations usually require a fast iterative method that does not require extremely high resolutions[29, 30]. However, this model is not adequate for representing the bath loading effects. Also, it fails in complex cases like atrial fibrillation where there are high wavefront curvatures, reentries, and wave collisions[31].

### 2.2.3 Forward Problem

Despite them being closely related, accurately representing the source model and calculating BSPs from cardiac sources can be distinguished as separate tasks. Even when the bath loading effect is ignored, it is feasible to derive a transfer matrix that maps the epicardial potentials to the torso surface. This matrix offers the possibility of skipping the cumbersome imaging and meshing processes for each individual patient[32]. However, this matrix would constitute a general mapping, overlooking the intricate physiological mechanisms beyond torso attenuation. Nevertheless, in addition to cardiac source modelling, there are many tools integrating a solution to forward problem and even in some cases to the inverse problem such as SCIRun[10, 33, 34, 35].

On the other hand, the structural components of the torso, including skeletal muscles, lungs, bones, and blood, are anticipated to influence the distribution and transmission of electrical signals within the torso. Including these heterogeneities in the thoracic region introduces an additional level of complexity to the solution of forward problem, while the benefits are controversial[36, 37, 38, 39, 40]. Irrespective of the inclusion of such heterogeneities, we introduce two numerical techniques, each offering distinct advantages in terms of heterogeneities and computational efficiency.

## Surface Methods

Surface methods, also known as boundary element methods (BEM), operate with the assumption that the torso consists of uniform regions with distinct conductivities, enclosed by closed surfaces as depicted in Fig. 2.3. The interaction between these surfaces is solved through the application of Green's second identity. The discretization of these surfaces is typically achieved using triangular meshes, and calculations are primarily focused on the vertices, aligning with the recommendations of Barr et al.[42].

In BEM, the transfer matrix ends up having a dense structure and it is calculated by iterative methods or elementary inversion when the matrix size is reasonably small. The singularity issue is avoided by deflating the transfer matrix and avoiding the problematic eigenvalue[41].

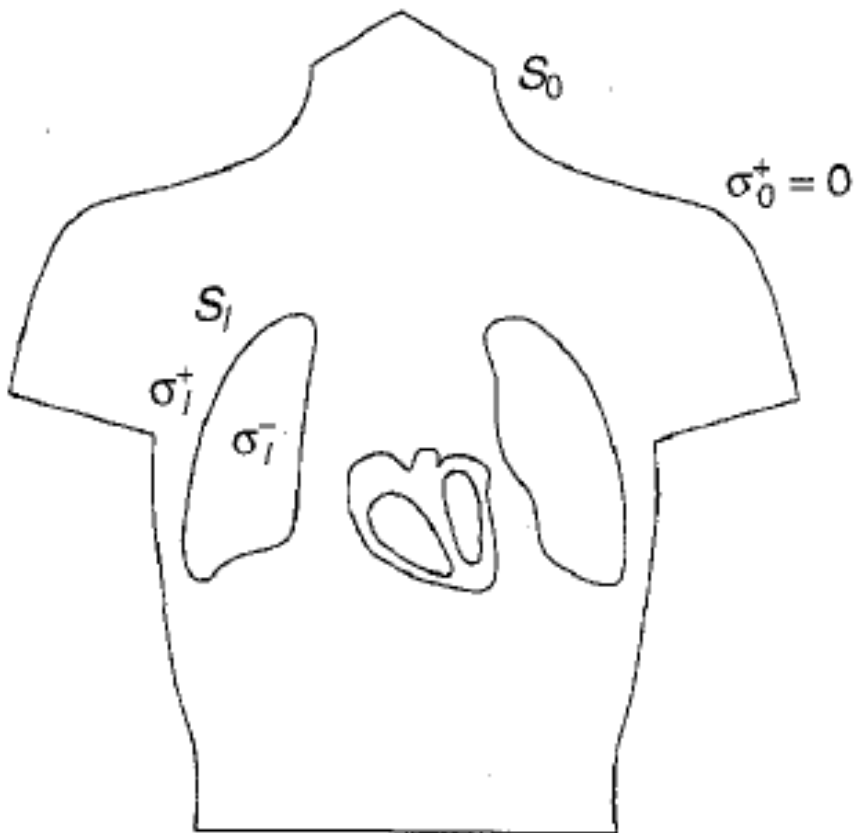


Figure 2.3: Torso with multiple regions of differing isotropic conductivity[41]

### Volume Methods

Volume methods involve the entire volume of the torso through tetrahedral and hexahedral elements. Kirchhoff's current law is formulated between these adjacent elements and then solved using Gauss-Seidel iteration. While the size of the coefficient matrix poses challenges in terms of storage and convergence speed, the matrix's sparsity enables the application of direct solvers built upon sparse matrix techniques[41].

## 2.3 Electrocardiogram

The discovery of cardiac activity's reflection on the torso surface dates back to 1887 when Waller observed potential alterations on human chest[43]. With his invention of string galvanometer, the father of ECG, Einthoven recorded electrical signals orig-

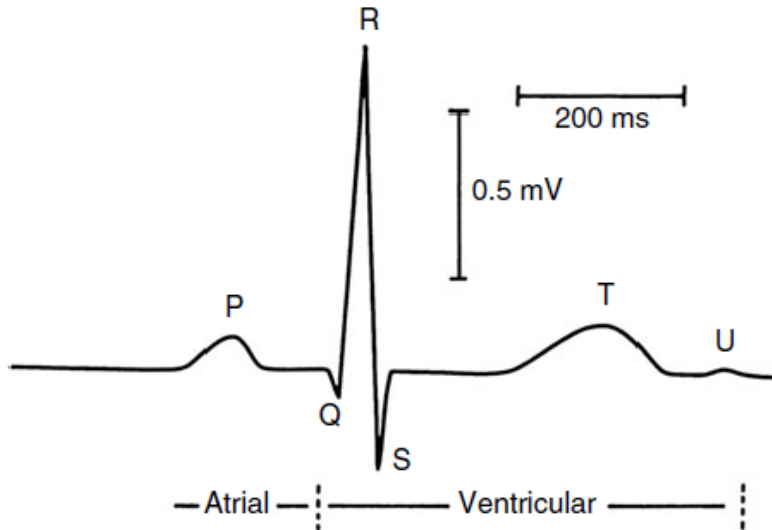


Figure 2.4: Peaks of a typical ECG waveform on Lead II[8]

inating from heart with high precision[44]. Furthermore, he labeled characteristic regions of typical ECG signal as shown in Fig. 2.4.

Due to the restricted sensitivity of recording equipment, early ECGs were recorded from individuals who had their hands or feet immersed in containers of saline solution. These solutions acted as electrodes thanks to their substantial contact with the skin. In the course of time, standard leads emerged taking the form shown in Fig. 2.5.

Wilson et al. recognized the limitations when all electrodes were distant from the heart. They introduced precordial leads using chest electrodes. Precordial lead voltages are measured relative to Wilson's central terminal, the average potential of three limbs, right arm, left arm, and left leg[45].

Now tilting the focus from the practical aspect to underlying electrophysiology, we need to comprehend the shapes of AP on different cardiac structures. Fig. 2.6 displays these APs, giving an insight into typical ECG patterns when combined with the dynamics of the torso. Furthermore, inspecting the regions of the ECG pattern shown in Fig. 2.4 would give us a deeper perspective on intrinsic CEP.

The ECG waveform features five distinct components, the P wave, the QRS complex, and the T wave. The P wave arises during the atrial depolarization phase, indicating the onset of atrial contraction, which typically commences about 25 ms after initiation. On the other hand, the QRS complex mirrors the ventricular depolarization, necessitating a stronger electrical signal due to the larger size of the ventricular cardiac muscle. As the QRS complex reaches its peak with the R wave, ventricular contraction initiates. Lastly, the T wave signifies ventricular repolarization. Importantly, atrial repolarization aligns with the QRS complex, making it indiscernible on the ECG recording [14].

Thanks to the patient-friendly application, non-invasive nature, and recent advancements in its interpretation 12-lead ECG is the most common clinical practice for cardiac abnormality diagnosis and monitoring today. Moreover, it remains to be one of the highlights of current research when it comes to cardiac risk stratification. There are numerous studies about ECG focusing on signal processing, instrumentation development, data interpretation, and cardiac model simulation. In the next chapter, we will be focusing on relevant work and attempt to give a vision of today's ECG research.

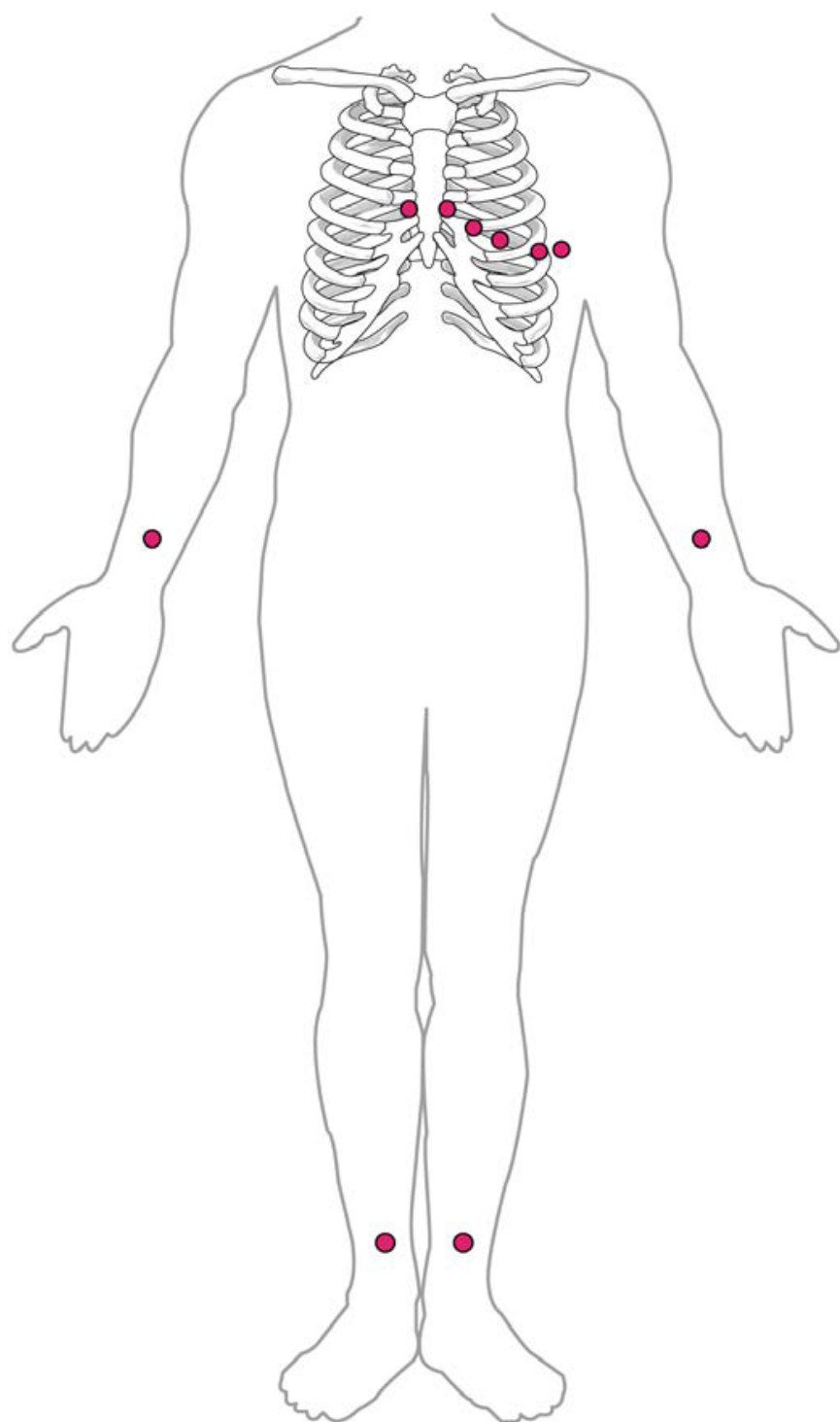


Figure 2.5: Standard lead positions[14]

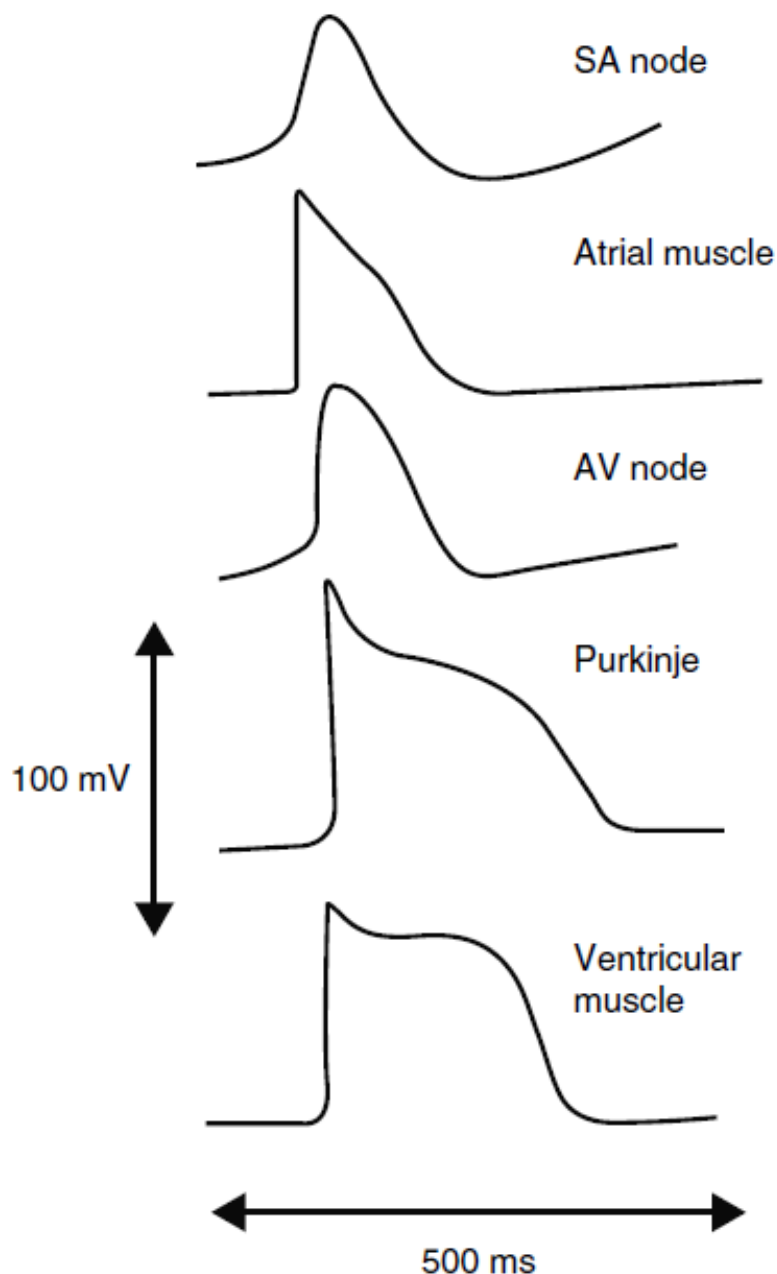


Figure 2.6: Characteristic APs drawn for different cardiac structures[8]

## 3 | Related Work

In this section, a comprehensive exploration of the current literature concerning CEP modeling with the goal of ECG generation is presented. This entails exhaustive scanning of the research related to the cardiac electrical activity simulation and further derivation of BSPs. Through this review, we align our study with the emerging trends, methodologies, and discoveries in the field. Later on in this chapter, the environment that has been employed for the simulation of ECG signals is demonstrated.

### 3.1 Modeling for ECG Interpretation

Especially with the recent advancements in data-hungry methods for the interpretation of biomedical signals and images, the need for physiologically relevant data has intensified. Adequately, CEP modeling studies started to accelerate responding to this demand since it is possible to obtain an enormous amount of clinically relevant data without the intervention on any animal or human subject. Specifically, the significant emergence of machine learning-based approaches for ECG interpretation aligned the focus of research to ECG simulation frameworks. Many tools like openCARP[10], acCELLerate[46], FEniCS[47], Chaste[48], LifeV[49], SCIRun[50], E-Cell[51], iCell[52], LabHEART[53], and CMISS[54] made an appearance for CEP simulations. The performance of the frameworks has been strongly dependent on the electrophysiological model for the cellular structure, the approach for the excitation propagation, and the method for the forward calculation. Also, despite us focusing on only the ECG generation in this study, whole BSP generation relating to an interesting research area of ECG imaging, has also become a performance criterion. Consequently, simulation durations ranged from seconds to hours for specific settings of the framework[55].

Although two types of simulations are intertwined, a clustering to healthy and pathological simulations is made for the review. It has to be noted that ECG simulation studies are not limited to direct simulations but many studies focus on verification and development of general CEP modeling with the focus of ECG generation[56, 57, 58, 59, 29, 60].

### 3.1.1 Healthy Heart Modelling

Various studies focus on different segments of the healthy ECG signal. In general, ECG signals are simulated by stimulation of the SA node or the ventricles. Therefore, resulting waveforms are accurately representing either traversal of AP through atria or the ventricles only. In the end, it is more convenient to focus on smaller intervals rather than the whole ECG pattern.

Along with clinical data, Cardone-Noott et al. studied the variability in activation speed and myocardial conductivities on modulating QRS width and amplitude through bidomain ECG simulations[61]. Kahlmann et al. developed a workflow calculating ECG through computer simulations and comparing the correlation with measured ECGs for parameter optimization. This parameter optimization resulted in a stimulation profile better matching the clinical scenario[62]. Furthermore, Cranford et al. performed an extensive sensitivity study evaluating the ventricular excitation pattern. Focusing on Purkinje-myocardial junctions (PMJs) where the stimulation is typically given for the ventricle-excited ECG simulations, they have reported on the optimal number and location of stimuli injection points[63].

In addition to the stimulation location, the patient anatomy is one of the key factors on the QRS complex pattern. Minchale et al. evaluated this effect through computer simulations run on 256 different models obtained through magnetic resonance imaging (MRI)[64]. On the other hand, Pezzuto et al. attempted to benefit the human anatomy along with 12-lead ECG recordings for accurate reconstruction of cardiac electrical activity[65].

As stated earlier, modelling studies are not limited to the QRS region. Xue et al. worked on the T wave morphology through the CEP simulations[66]. Similarly, Keller et al. examined the influence of ionic flow heterogeneities on T wave genesis[67]. In another study, Moss et al. assessed how different phases of the contraction cycle affect the T wave properties[68]. The P wave was also produced through monodomain simulations with 1000 dipoles distributed throughout the atrial mid-myocardium[69]. Inaccuracies between electrocardiology literature and computer simulation results for P waves are discussed through comparison[70]. The impact of the atrial activation site and left atrial size on P wave morphology was studied by Loewe et al. and Andlauer et al., respectively[71, 72].

### 3.1.2 Abnormal Heart Modelling

The literature on healthy heart modeling represents merely the visible tip of the iceberg. A significantly more extensive range of modeling has been undertaken for pathological hearts. A detailed review of these studies is far beyond the scope of this thesis and the reader is kindly referred to Dossel et al.'s review [55], where they classified studies into the following subgroups:

- Ischemia and Infarction
- Ventricular Ectopic Beats and Extrasystoles

- Ventricular Tachycardia
- Cardiomyopathy
- Bundle Branch Blocks
- Atrial Ectopic Beats
- Atrial Tachycardia, Flutter and Fibrillation
- Genetic Diseases and Channelopathies
- Imbalance of Electrolytes
- Drug-Induced Changes in the ECG

## 3.2 openCARP

Now that the available literature on CEP model development for ECG generation has been outlined, we tilt our attention to the specific framework of our interest. openCARP is a sophisticated simulation environment for advanced in silico experiments in CEP. In essence, it is designed to be able to replicate and build on the majority of available CEP studies. Its platform is constructed upon the foundation of its predecessors, CARP and acCELLerate. openCARP offers a user-friendly and flexible interface in combination with the *carputils* framework even for those who are not familiar with computational simulations. Thus, openCARP enhances the utilization, transparency, standardization, and reproducibility of in silico CEP experiments[10].

Although openCARP is designed to be an environment for CEP simulations, it does not provide an out-of-the-box tool for ECG generation. Rather, it provides the building blocks for simulations and expects the user to bring them together depending on their specific need. In the next chapter, openCARP environment is unrevealed through the description of these building blocks. Therefore, in this section, we are not going through the detailed description of the environment, and the reader is kindly referred to Ch.4 for it. Rather, some recent publications utilizing openCARP are presented in the upcoming paragraph.

Despite its release in March 2020, openCARP has been cited by more than 70 publications as of September 2023. Again, it is out of our scope to review all of these studies but some relevant ones are as follows. Probably the most comprehensive study performed with openCARP so far is the one performed by Nagel et al. where they compare the propagation models and forward calculation methods on cellular, tissue and organ scale in atrial electrophysiology[23]. A very interesting study focusing on maternal-fetal ECG for diagnosis of congenital heart disease was performed manipulating the flexibility of openCARP[73]. The developers utilized their tool for the derivation of P waves in another recent study[74]. Again the developers modified

the previously described eikonal model for faster arrhythmia simulations[75]. openCARP has also been used for the verification of an open-source software pipeline to create patient-specific left atrial models with fiber orientations and a fibrosis map[76]. Although its pipeline is not completely public, a data set of 16,900 healthy and pathological 12-lead ECGs has been made publicly available where all the simulations are claimed to be reproducible with openCARP framework[77]. Pushing the limits of current literature, a personalized real-time virtual model of whole heart electrophysiology model is developed by Gilette et al.[78].

# 4 | Materials and Methods

The openCARP environment provides powerful tools for CEP modeling. Within this framework, the electrophysiology of a single cell or the electrophysiology of the tissue can be simulated. However, these simulations primarily address individual characteristics and experiments, rather than capturing physiological dynamics as a whole. Moreover, the provided tools are not extended to support organ- or system-level simulations. The user is expected to bring strictly restricted simulation blocks that focus on only a single dynamic of CEP and develop their own model for a comprehensive simulation. Unfortunately, neither openCARP environment nor the available literature provides a blueprint of how to accomplish this. Therefore, aiming at simulation of system-level behavior of a beating heart, we had to dive deep into the source code of openCARP, understand the relationships of different functions, and construct a simulation pipeline from scratch.

In this study, our starting point was the investigation of examples that explore individual dynamics of heart tissue electrophysiology. These examples were based on block tissue structures that do not reflect the clinical geometry of the heart. For that reason, these examples are tailored to reflect the organ-level characterization. Subsequently, these adapted examples are converted to foundational components of the system-level simulation framework. Alongside, the missing components of the framework are designed from the ground up with the intricate understanding of openCARP and *carputils* functions. Lastly, all of the components for whole heart simulation are integrated and optimized for the generation of ECG signals.

In this section, the elements integrated and the methods followed are introduced. The simulation material that is employed is presented along with the rationale behind the parameter and setting selections referring to the related literature. Moreover, concise code excerpts are provided to facilitate the reproduction of the results. Lastly, details regarding visualization are outlined, providing readers with a glimpse of what to expect in the forthcoming chapter.

## 4.1 Source Model

The first consideration point for ECG derivations through CEP simulations is the source model. It is important to clarify the notation that source and propagation model refer to the same issue. They have been used interchangeably in literature and openCARP environment denotes it as source model.

There is a consensus about the source model choice when it comes to ECG interpretation on bidomain model since other models fail to accurately include concomitant current flow effects. Therefore, despite the high computational costs, bidomain model is the established gold standard for forward electrophysiological modeling[29, 23, 26]. In this work, matching with the state-of-the-art, we have committed to the use of bidomain formulation for our calculations. openCARP demonstrates notable competence in furnishing this configuration for the source model.

## 4.2 Meshes

The first circumstance arising from the choice of bidomain source model is the need for an accurate representation of the regions outside the heart. In CEP simulations this area can generally be referred as bath or torso. Bidomain model is the superior model in terms of precise reflection of the bath-loading effects although it is commonly ignored in CEP models due to the high computational costs[79]. In our study, whole torso mesh structure has been used for exact representation of the bath region.

In total, two torso geometries are included in the scope of this work. These geometries are adapted from the study of Qian et al. where they investigated implantable cardioverter defibrillator generator placement configurations. Finite element mesh of torso structures were generated using Simpleware, producing meshes with average edge lengths of  $800\pm50 \mu m$  for left ventricle (LV) and right ventricle (RV) free walls,  $2\pm1 mm$  for organs and other non-myocardium regions, and  $2\pm1.5 mm$  for all coils and cans[80]. Coils and cans refer to defibrillator equipment that are taken as a part of homogeneous torso in our study. So, it can be claimed that the torso mesh is adjusted for completely healthy torso characteristics since it does not include disturbances caused by the equipment included in the mesh.

LV and RV cardiac fiber architecture is reconstructed in a rule-based approach[81]. Unfortunately, atria do not include the fiber orientations limiting this study in terms of whole ECG pattern generation. Due to this limitation P wave cannot be reconstructed mainly relating to the fact that the P wave is caused by the electrical activation traversal through atria[14].

The meshes are resampled to decrease the computational duration. Meshtool developed by Neic et al. is utilized for the resampling process. The resolutions of the volume meshes are decreased by adjusting average lengths using iterative edge-bisection algorithm[82]. The resampling algorithm consists of two primary steps. First, edges longer than the defined maximum size threshold are split. Then, edges smaller than the designated minimum size threshold are collapsed. However, certain edges might not be subject to collapsing due to quality considerations, leaving some edges smaller than the defined minimum edge size[83].

An example script for resampling is given to provide a framework eligible for other mesh structures that are not used in this study:

---

```
./meshtool resample mesh
-msh=/path/to/original/mesh
-min=3000
-outmsh=/path/to/resampled/mesh
-surf_corr=0.95
```

Following script displays the details of the edge attributes:

```
./meshtool query edges
-msh=/path/to/resampled/mesh
```

Myocardium structure is needed to be extracted from the torso mesh to visualize the transmembrane potentials arising from monodomain simulations. Meshtool has a specific myocardium extraction function that extracts regions of the mesh having a nonuniform fiber orientation[83]. The script for such a task is as follows:

```
./meshtool extract myocard
-msh=/path/to/original/mesh
-submsh=/path/to/extracted/myocardium/mesh
```

## 4.3 Regions

The mesh folder typically has three distinct files with extensions \*.pts, \*.ion, and \*.elem. \*.pts file outlines the locations of vertices and \*.ion file describes the fiber orientation that has been mentioned so far. On the other hand, \*.elem file enables the registering of different CEP parameters to the different regions of the mesh. In particular, the distinction between myocardial tissue and the bath is made by assigning different electrophysiology to the labeled regions. Furthermore, despite us not including such heterogeneities in cardiac tissue, for instance, ischemia regions can be introduced by assigning lower conductivity values to distinct areas on ventricles or atria. In this study, we have made the separation of left and right ventricles from other tissue including blood, muscles, organs, lungs, and further inhomogeneities of the torso that are considered as bath.

### 4.3.1 Ionic Model

Library of IMPs (Ionic Model & Plug-ins) for Electrophysiological Theorization (LIMPET) is a library introduced in openCARP environment to keep a consistent interface for a set of efficiently implemented ionic models. In addition to the models in this library, openCARP allows custom models to be introduced to the simulation framework. By doing so, it provides flexibility for users to integrate their pathological cell models into the simulations.

In our study, we have chosen two different ionic models that are built within the openCARP environment. These models are chosen because they are the ones

appearing the most in the examples provided by openCARP. Since our building blocks are partly based on these examples the models are selected appropriately.

The first model was developed employing specific formulations of the  $K^{+1}$ ,  $Na^{+1}$ , and  $Ca^{+2}$  currents derived from human atrial myocytes. Furthermore, pump, exchange, and background currents were incorporated for the mathematical formulation of AP. This first ionic model is referred as Courtemanche, named after its developer[84].

The second model was constructed by ten Tusscher et al. This model was based on human ventricle tissue and it was also built within the openCARP environment. A detailed comparison highlighting the modeling steps is given within the description of the tenTusscherPanfilov model during its introduction[85]. Moreover, a meta-analysis between electrophysiology computational models is given by Niederer et al.[86].

### 4.3.2 Conductivities

The assignment of correct conductivity levels to related regions is vital for a converging simulation. Although the conductivity levels for the regions are given along with the meshes, two important factors are overseen if one directly adapts these values. Firstly, the inhomogeneities of the torso are ignored within the scope of this study. Therefore, 33 different conductivity levels for each torso structure are redundant. Secondly, the meshes are resampled resulting in various resolutions warranting the scaling of the conductivity coefficients.

Besides, assigned conductivity levels must be comparable with other experiments using different methodologies that are based on CV rather than the conductivity tensor. Moreover, conductivity levels are dependent on the ionic model of the heart. At this juncture, openCARP provides a tuning tool for conductivity adjustment. Within an iterative scheme proposed by Costa et al., tuneCV function scales the intracellular and extracellular conductivities reported in earlier literature to match the desired CV for specific resolution and ionic model[87, 88, 10]. In our study, we tried to achieve CV reported by Caldwell et al. with a  $1,000 \mu m$  resolution[89]. Further on, calculated CVs are scaled again depending on the mesh resolution and excitation site.

Sample script for tuning conductivities with tuneCV function is given. Base conductivity values obtained are also reported after the script.

```
tuneCV
--converge true
--tol 0.0001
--velocity 0.67
--model Courtemanche
--sourceModel bidomain
--resolution 1000.0
```

```
Conduction velocity: 0.6701 m/s [gi=0.7433, ge=2.6700, gm=0.5815]
```

```
tuneCV
--converge true
--tol 0.0001
--velocity 0.30
--model Courtemanche
--sourceModel bidomain
--resolution 1000.0
```

```
Conduction velocity: 0.3042 m/s [gi=0.2981, ge=1.0707, gm=0.2332]
```

```
tuneCV
--converge true
--tol 0.0001
--velocity 0.17
--model Courtemanche
--sourceModel bidomain
--resolution 1000.0
```

```
Conduction velocity: 0.1587 m/s [gi=0.1512, ge=0.5430, gm=0.1182]
```

### 4.3.3 Bath

Torso mesh structure that is used in this study includes 33 distinct torso elements. Since this level of detail is considered redundant for BSP calculations and thereby ECG calculations, the complexity is decreased by assuming all the elements other than LV and RV as torso bath[36]. A bath conductivity of 0.7 S/m is assumed according to the conductivity values given for the elements of torso[80].

## 4.4 Stimuli

The initiation of electrical activity is normally sustained by the SA node in a healthy heart. In cardiac simulations, this initiation is manually maintained unless SA node modelling is a consideration. The optimal stimulation is usually dependent on the specific pathology that is being studied. In our case, we are simulating a healthy heart that is usually stimulated from the PMJs. An extensive sensitivity study by Cranford et al. concluded by claiming the QRS complex features are most sensitive to the locations of a few well-placed stimuli rather than to the sheer number of stimuli[63]. Trying to replicate their activation points shown in Fig. 4.1, we stimulated the heart from a single point that is closest to septum on epicardial surface.

#### 4.4.1 Stimulus Type

openCARP allows multiple types of stimulus circuits like transmembrane current, extracellular current, extracellular voltage,  $V_m$  clamp, and so on. In this study, the stimulation circuit has been limited to transmembrane current with  $250 \mu A/cm^2$  amplitude.

#### 4.4.2 Stimulus Location

Vertex-based stimulus definitions require a \*.vtx file within the openCARP simulation environment. The contents of the \*.vtx file are the number of nodes belonging to the volume element that we want to stimulate from and the stimulus domain followed with the nodes of the volume element. An example \*.vtx file can be given as:

```
4
extra
65768
59629
60071
61656
```

### 4.5 Leads

Standard lead configuration for the calculation of 12-lead ECG has been used. Leads that are supposed to be on the limbs are put to the extremities of the torso. Fig. 4.2 depicts the locations of the electrodes. Right leg is usually taken as ground and since unipolar electrodes are used, a reading from the right leg was not required.

#### 4.5.1 Lead Identification

In each individual mesh structure, the identification of lead positions is a tedious task. Especially for the precordial electrodes, anatomically accurate placement of electrodes is influential on ECG readings. In this study, the identification of lead positions is assisted by two physicians. However, since the original placement of ECG electrodes is not provided along with mesh structures, the precision of lead locations is controversial.

#### 4.5.2 ECG Calculation

12-lead ECG recordings are derived by simple mathematical manipulation of 9 electrode recordings. These electrode recordings are named as right arm (RA), left arm (LA), left leg(LL), and precordial electrodes V1, V2, V3, V4, V5, and V6. Leads are derived by following equations[91, 90]:

$$\text{Lead } I = LA - RA \quad (4.1)$$

$$\text{Lead } II = LL - RA \quad (4.2)$$

$$\text{Lead } III = LL - LA \quad (4.3)$$

$$\text{Lead } aVR = RA - 0.5 * (LA + LL) \quad (4.4)$$

$$\text{Lead } aVL = LA - 0.5 * (RA + LL) \quad (4.5)$$

$$\text{Lead } aVF = LL - 0.5 * (RA + LA) \quad (4.6)$$

The chest electrodes are calculated by subtracting the Wilson's central terminal from unipolar precordial recordings. The Wilson's central terminal is calculated with the following equation[45]:

$$WCT = (LA + RA + LL)/3 \quad (4.7)$$

## 4.6 Simulator Options

Domain definitions are critical in openCARP. Extracellular and intracellular spaces should be assigned to correct electrical domains as well as the stimulus. For instance, if intracellular current stimulus is chosen for the circuit type, one should make sure that the volume element that is being stimulated is inside the intracellular electric domain.

Another significant consideration factor for openCARP simulations is the time step to solve the numeric equations for. Naturally, smaller time steps result in longer computation times whereas the choice of too large time step causes simulations to fail. 0.4 ms has been found to be the bare minimum for successful simulations, empirically. Although it does not necessarily have to be the same, the output frequency consequently became 2500 Hz.

## 4.7 Visualization

Another essential component of openCARP environment is its visualization tool, Meshalyzer[10]. Meshalyzer is capable of displaying transmembrane and extracellular potentials on given mesh structures dynamically. Also, it is possible to observe time series of selected vertices. Local ATs can be mapped on cardiac structures. Using this precious tool, we are presenting potential distributions at certain time instants in the next chapter. These time instants are carefully chosen to reflect the depolarization and repolarization phases in necessary but not overwhelming detail.

Another useful tool for visualization that we facilitated is gnuplot[92]. ECG plots are obtained by gnuplot with lines. Furthermore, correlation coefficients are calculated for Lead II between runs having different parameter settings. An example code excerpt for the generation of ECG lead plots is given as follows:

```
set terminal wxt size 700, 900
set multiplot layout 6, 1
set ylabel 'voltage (mV)'
plot 'Lead1.dat' using ($0/2.5):1 t "I" with lines lw 3
plot 'Lead2.dat' using ($0/2.5):1 t "II" with lines lw 3
plot 'Lead3.dat' using ($0/2.5):1 t "III" with lines lw 3
plot 'LeadaVR.dat' using ($0/2.5):1 t "aVR" with lines lw 3
plot 'LeadaVL.dat' using ($0/2.5):1 t "aVL" with lines lw 3
set xlabel 'time (ms)'
plot 'LeadaVF.dat' using ($0/2.5):1 t "aVF" with lines lw 3
unset multiplot
```

## 4.8 Writing

The writing process is aided by figure creation, proofreading, and citation management applications. Specifically, Inkspace 1.3 has been used for the creation of the figures. The proofreading is done by the app named Grammarly. Lastly, the citations are managed using the tool Mendeley.

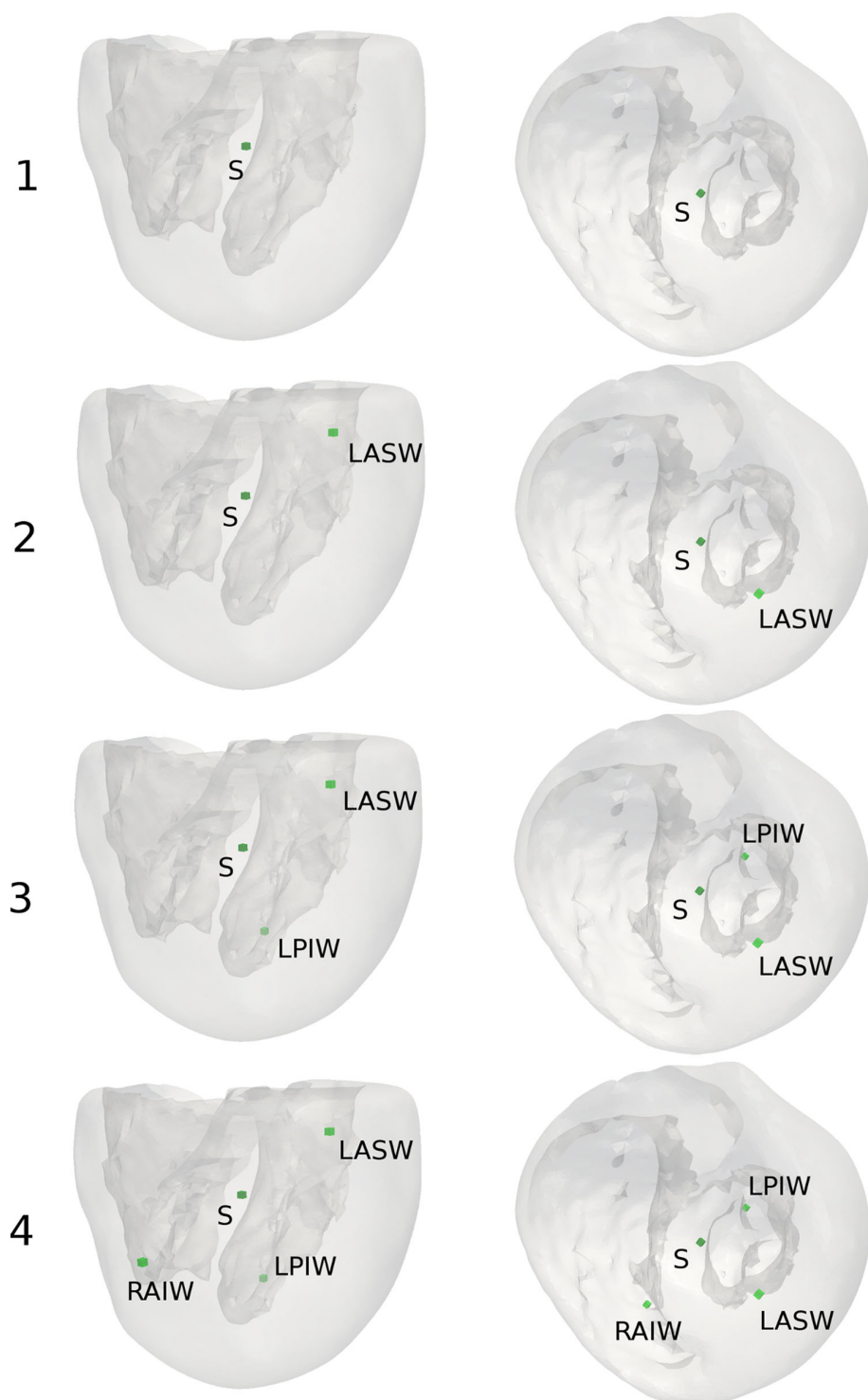


Figure 4.1: Locations of the most sensitive stimuli reported by Cranford et al.[63]

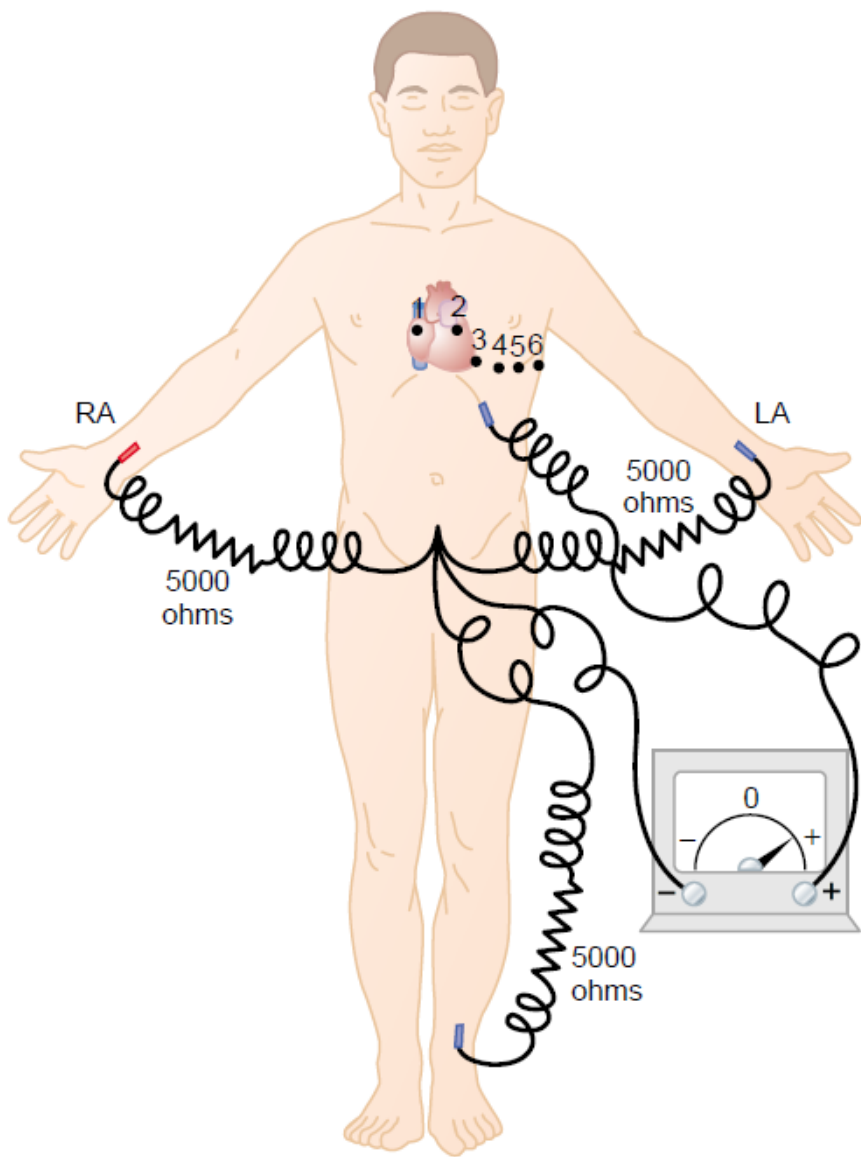


Figure 4.2: Locations of the leads[90]

# 5 | Results

The simulation outcomes are presented in this chapter. Firstly, a sample run is outlined to have a common ground. Later, in each section, the effect of a setting change is demonstrated. The command that is run in the terminal has been modified to include these changes explicitly and given as:

```
./run.py  
--sourceModel bidomain  
--duration 500  
--meshname KCL_torso1_resampled_min3000  
--stimname stim1min3000.vtx  
--conductivityfactor 6  
--bathconductivity 0.7  
--ionicmodel Courtemanche  
--dt 400
```

## 5.1 Sample Run

The sample model is simulated using the bidomain source model. The duration of the simulation is kept constant in all runs to 500 *ms* for visualization of the whole repolarization segment. The mesh structure is chosen as the first torso mesh provided by Qian et al.[80]. This mesh is resampled to an average edge length of 4,895  $\mu m$ . Stimulation location is selected near the apex of the heart on the LV. The conductivity factor that scales the conductivity coefficients is found to be 6 along with a bath conductivity of 0.7  $S/m$ . The base ionic model is decided to be Courtemanche and finally, ECG frequency became 2,500  $Hz$ .

Firstly, the BSP map can be seen in Fig. 5.1. On the left column of this figure time spacings are chosen smaller compared to the right column to visualize the depolarization in satisfactory detail. While the depolarization sequence is observed on the left column, careful inspection of the left column allows the detection of the T wave as extracellular potentials reach a peak around t=270ms.

Secondly, Fig. 5.2 depicts the extracellular potential readings on the epicardial surface. Similar to Fig. 5.1, time spacings are adjusted for a clear depiction of activation propagation. Indeed, the left column of the figure clearly indicates how the APs are propagating through ventricles from the apex to the base of the heart.

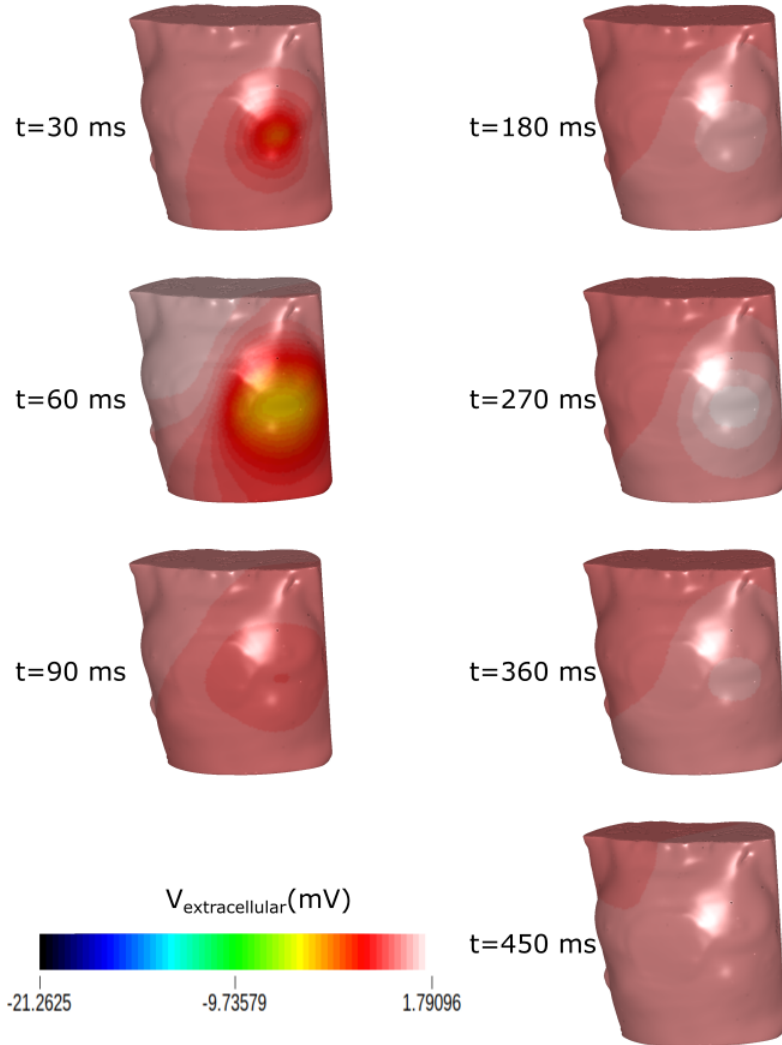


Figure 5.1: Extracellular potentials of the torso in the sample run

Moreover, Fig. 5.3 depicts the transmembrane voltage readings from the apex, free wall, and the base of the heart, conforming with the typical AP shape.

Thirdly, Figures 5.4 and 5.5 portray the 12-lead ECG readings for limb and chest electrodes, respectively. The sharp depolarization pattern and in a later stage, a softer repolarization shape are seen on all the leads.

Lastly, AT map for the heart is shown in Fig. 5.6. The activation threshold is chosen as  $-10 \text{ mV}$  and the time scale is in  $\text{ms}$ . Furthermore, transmembrane potentials are shown as a part of Fig. 5.7 therefore not explicitly plotted in a separate figure.

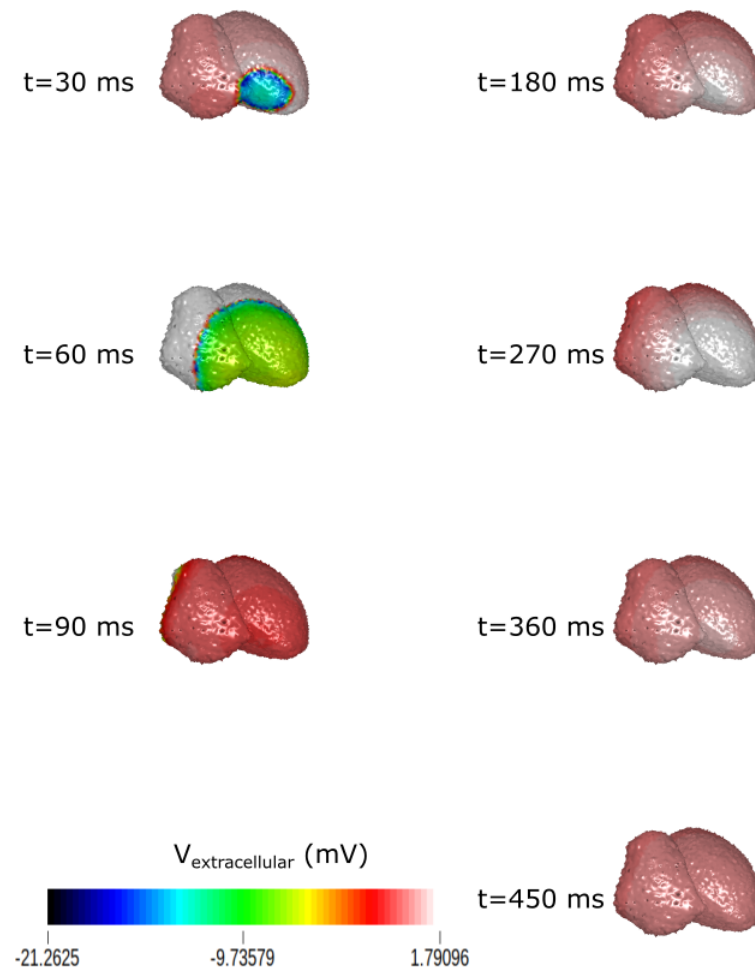


Figure 5.2: Extracellular potentials of the heart in the sample run

## 5.2 Source Model

Extracellular potentials are not calculated for the whole torso surface when a source model of monodomain is used. However, transmembrane voltages are calculated for all source models used in this study. Fig. 5.7 depicts the measured transmembrane voltage levels of three time instances belonging to the depolarization phase for three source models. The pseudobidomain model required a different conductivity factor than the two others for a successful simulation. Therefore, the activation wavefront is lagging on it. Although the same conductivity factor is used for monodomain and bidomain models, wavefront of the monodomain model is also slightly lagging compared with the wavefront of the bidomain model.

One of the most important consideration points in choosing the source model

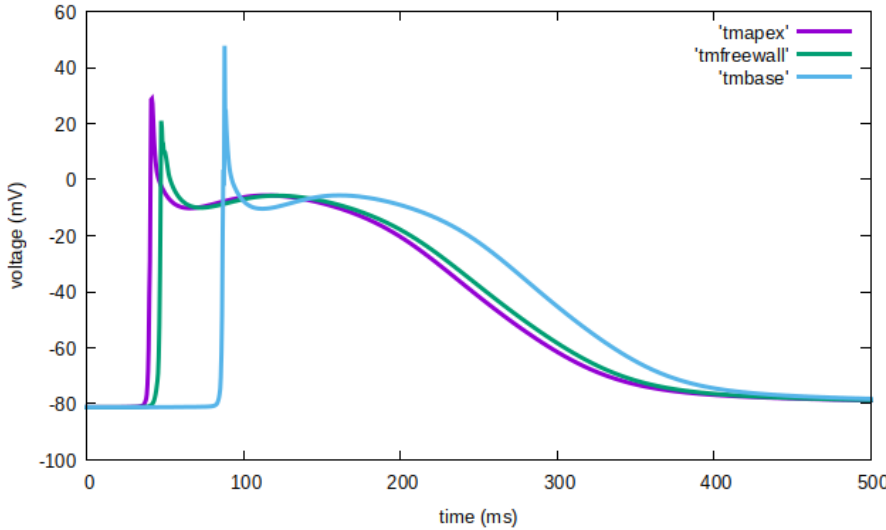


Figure 5.3: Transmembrane potentials of three different points on the epicardial surface in the sample run. Three points are chosen from the apex, LV freewall, and base of the heart.

Source Model	Computation Duration (sec)
Monodomain	26
Pseudobidomain	2,587
Bidomain	2,886

Table 5.1: Computation durations for the simulation of one heart cycle in different source models

is the computational cost. Table 5.1 indicates the computation durations for the simulation of one heart cycle on a Linux-based machine having an Intel(R) Xeon(R) CPU E5-1650 v4 @ 3.60GHz and 64 GB RAM.

## 5.3 Resampling

The computational concerns led us to resample torso meshes to a smaller mean edge length. However, the simulation quality must be preserved. With this aim, we compared the simulation performances when the torso structure is resampled with a target mean edge length of 3,000, 5,000, and 10,000  $\mu\text{m}$ . The resampling tasks are performed using meshalyzer with the methods outlined in the previous chapter. This task resulted in mean edge lengths and file sizes given in Table 5.2.

The BSP patterns as shown in Fig. 5.8 do not show significant differences with changing resampling rates. Further assessment of 12-lead ECG recordings in Figures 5.9 and 5.10 also present only modest discrepancies between mesh structures resampled to target mean edge lengths of 3,000 and 5,000  $\mu\text{m}$ . Therefore, after extensive

Target Mean Edge Length (um)	Resampled Mean Edge Length (um)	Size of openCARP Files (MB)	Computation Duration (sec)
3,000	4,895	125.7	2,886
5,000	6,580	51.9	1,103
10,000	6,895	31.5	522

Table 5.2: Mesh properties and computation durations for the simulation of one heart cycle in meshes resampled to different target mean edge lengths

Mesh	Stimulation Location	Ionic Model	Conductivity Factor	Bath Conductivity (S/m)	Correlation Coefficient
Torso 1	RV	Courtemanche	7	0.7	1
Torso 2	RV	Courtemanche	3	0.7	0.5444
Torso 1	RV	tenTusscherPanfilov	7	0.7	0.7512
Torso 1	RV	Courtemanche	8	0.7	0.9736
Torso 1	RV	Courtemanche	7	1	0.9999
Torso 1	LV	Courtemanche	7	0.7	0.966

Table 5.3: Correlation coefficients for various simulation settings

inspection of the resampling, we decided on the base model as the one resampled to an average edge length of  $6,580 \mu m$  to decrease the computational duration for the generation of one heart cycle in further simulations. This mesh allows us to compare setting changes in convenient computational durations.

## 5.4 Mesh

Torso geometry is one of the most important contemplation points for ECG simulations. The physiological structure of the torso has an inevitable effect on the ECG measurements. To see the diversity between different torso geometries, 12-lead ECG is simulated on two different torso structures selected from the study of Qian et al. The first two torso computational models provided in their study are both resampled to the same target mean edge length[80]. Fig. 5.11 illustrates extracellular BSPs of these two meshes. It has to be reminded that since we use a basis conductivity tensor pair calculated for meshes having  $1,000 \mu m$  mean edge length we scale these tensors with a conductivity factor. And, since the two different torso structures end up having nonidentical mean edge lengths, they require the use of different conductivity factors. Hence, in addition to the differentiated propagation patterns on the torso, AT maps also differ.

Using the base mesh model and the simulation settings given in the first line of Table 5.3, a base experiment is performed. Later, for the output of the specific run, a correlation coefficient between the base experiment and the specific run is calculated. This coefficient displays how similar the ECG patterns on Lead II are with the base run. In Table 5.3, every row portrays only a single setting change while keeping all the others controlled.

## 5.5 Ionic Model

In the scope of this study, the Courtemanche ionic model is chosen as the main ionic model formulating the relations of ionic currents and membrane voltages. To inspect the effect of simulations with other ionic models the tenTusscherPanfilov model is also utilized while controlling all the other parameters. Fig. 5.12 displays the extracellular potentials on the epicardial surface for a time instance belonging to the depolarization phase for two different ionic models side by side. In the tenTusscherPanfilov ionic model-based simulation, the wavefront appears to travel faster despite using the same conductivity tensors. Indeed, conductivity tensors are also ionic model dependent, and to achieve the same CV, conductivity tensors must be calculated based on the ionic model in hand.

The lagging wavefront can be observed in limb and chest lead measurements as well. Furthermore, careful examination of Figures 5.13 and 5.14 indicate more pronounced depolarization and repolarization waves. Readjustment of conductivity tensor might mitigate this discrepancy causing correlation coefficients for Lead II as low as 0.7512.

## 5.6 Conductivity Factor

An external conductivity factor that scales all the conductivity coefficients is incorporated to be able to run simulations that converge. As in tuneCV function, a conductivity factor that allows the simulation to converge is chosen for each mesh structure, iteratively. Naturally, a useful utility of this factor became changing the CVs. By scaling the conductivity factor from 7 to 8 we can clearly observe faster propagation of electrical stimulus through the epicardial surface by checking Figures 5.15 and 5.16. Moreover, Figures 5.17 and 5.18 are portraying the shift in the same wave pattern caused by conductivity scaling on all limb and precordial leads.

## 5.7 Bath Conductivity

Presumed bath conductivity remains to be a controversial topic in ECG simulations. To see the effect we assigned two different values for the uniform bath conductivity and observed insignificant alterations. Nevertheless, a detailed comparison of epicardial potentials in Fig. 5.19 proves that the bidomain source model accounts for the bath-loading effects. Depiction of BSP distributions yielded insignificant variations between two conductivity levels in Fig. 5.20.

## 5.8 Stimulus Location

Electrical impulses originate from the stimulation point. Alterations of stimulation location might indicate a specific type of pacing or pathology depending on the

clinical relevancy. In the scope of this thesis, ventricles are paced from the right and left ventricles. In Figures 5.21 and 5.22 the impact of the stimulation point on the torso and heart surface extracellular potential distributions are presented. The focus shifted toward the center on the torso with the stimulation point being moved to the RV.

AT maps shown in Fig. 5.23 clearly indicate how stimulus location has been varied. In Figures 5.24 and 5.25 the diversity introduced to ECG patterns is shown. Despite some leads still staying correlated, Lead I, aVL, and V1 showed significant differentiations from the base model.

## 5.9 Time Step

The time step to solve the numeric equations for is crucial for convergent simulations.  $400 \mu s$  is found to be the lower limit for simulations having our settings. The frequency of ECG measurements is increased by decreasing the time step to 100 and  $200 \mu s$ . The comparison between ECG measurements having frequencies of 2,500 and 10,000  $Hz$  is portrayed in Figures 5.26 and 5.27. The effect of change in time step has been observed not only limited to resolution but also the shape of the pattern.

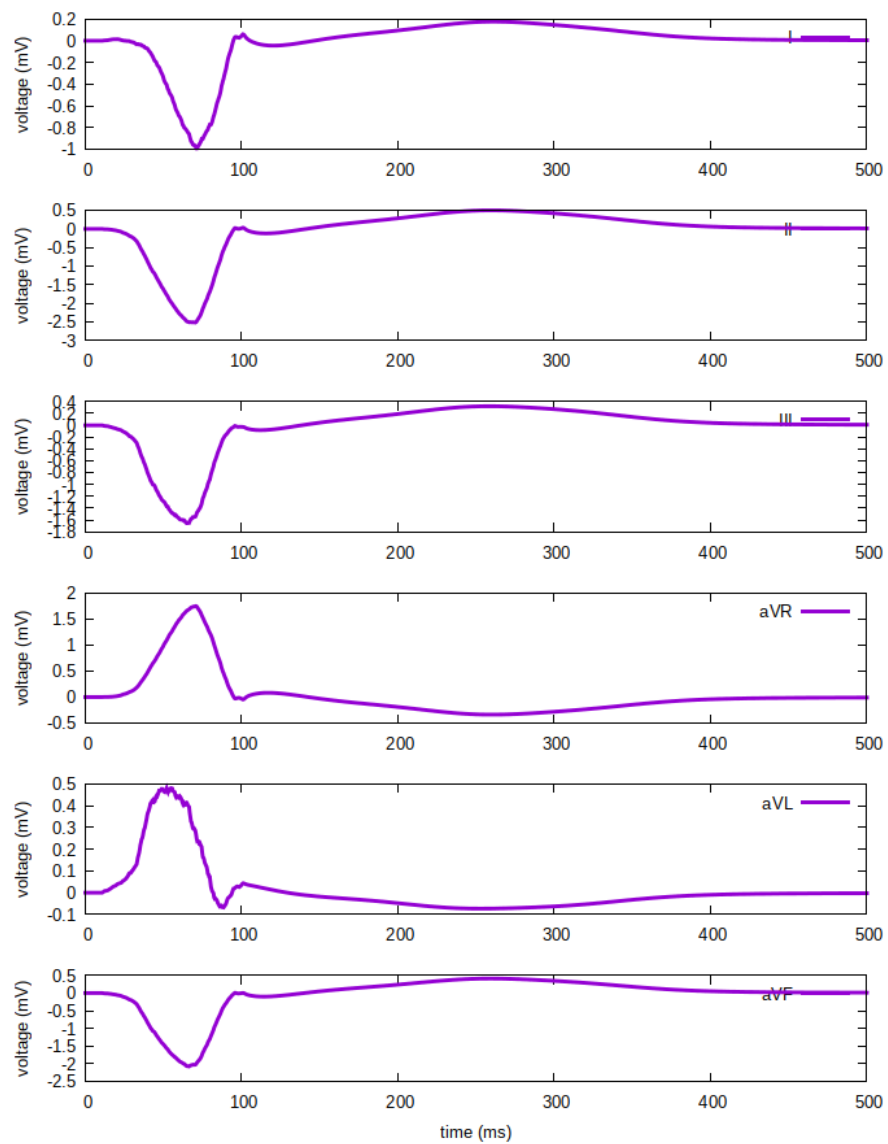


Figure 5.4: Limb leads ECG measurements of the sample run

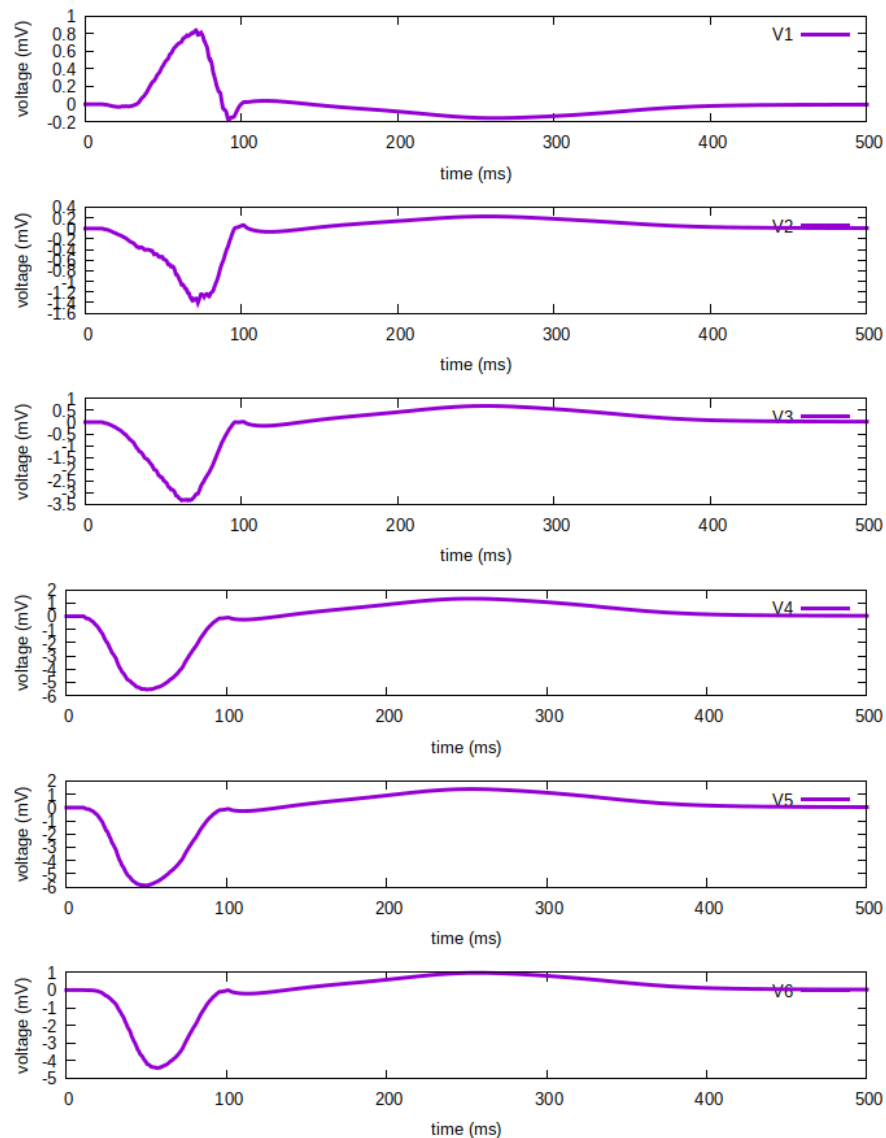


Figure 5.5: Chest leads ECG measurements of the sample run

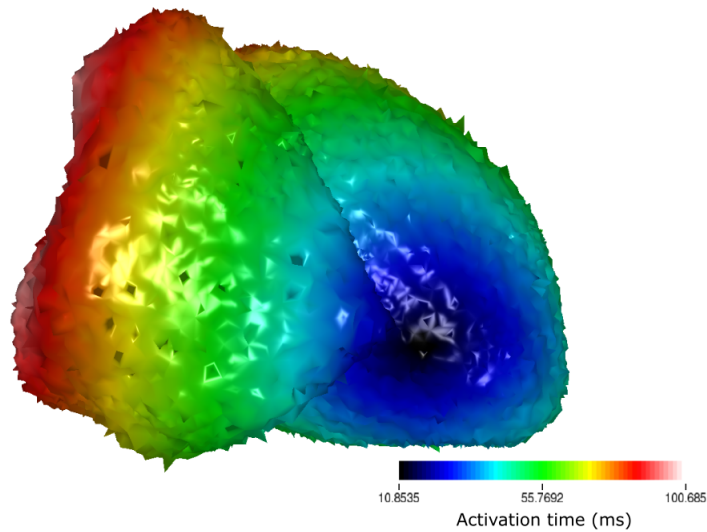


Figure 5.6: AT map of the sample run. Nodes are assigned with time instants corresponding to the moment they cross the threshold potential.

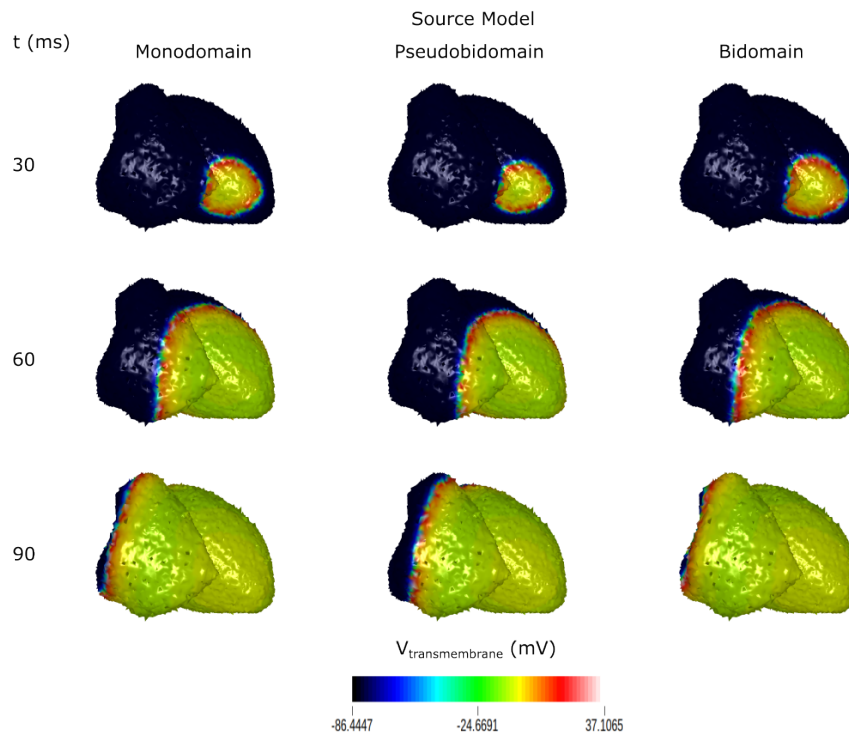


Figure 5.7: Transmembrane potentials of the heart simulated with different source models

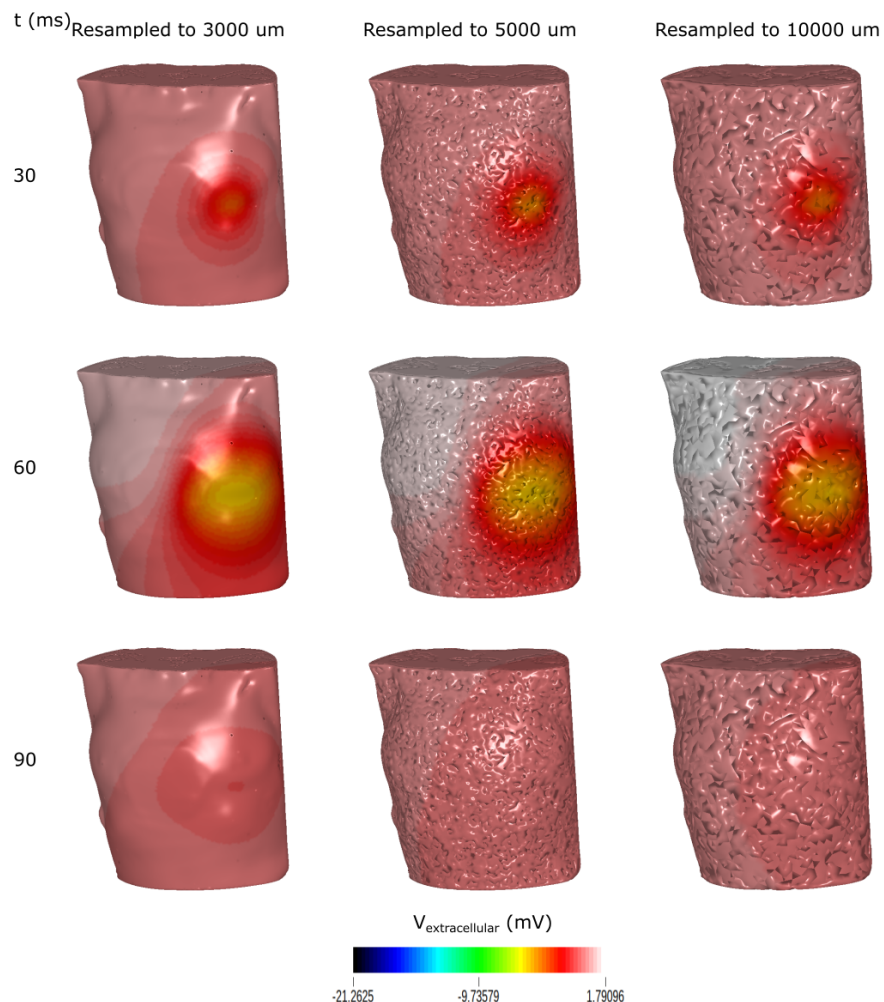


Figure 5.8: Extracellular potentials of the torso simulated with meshes having different resampling rates

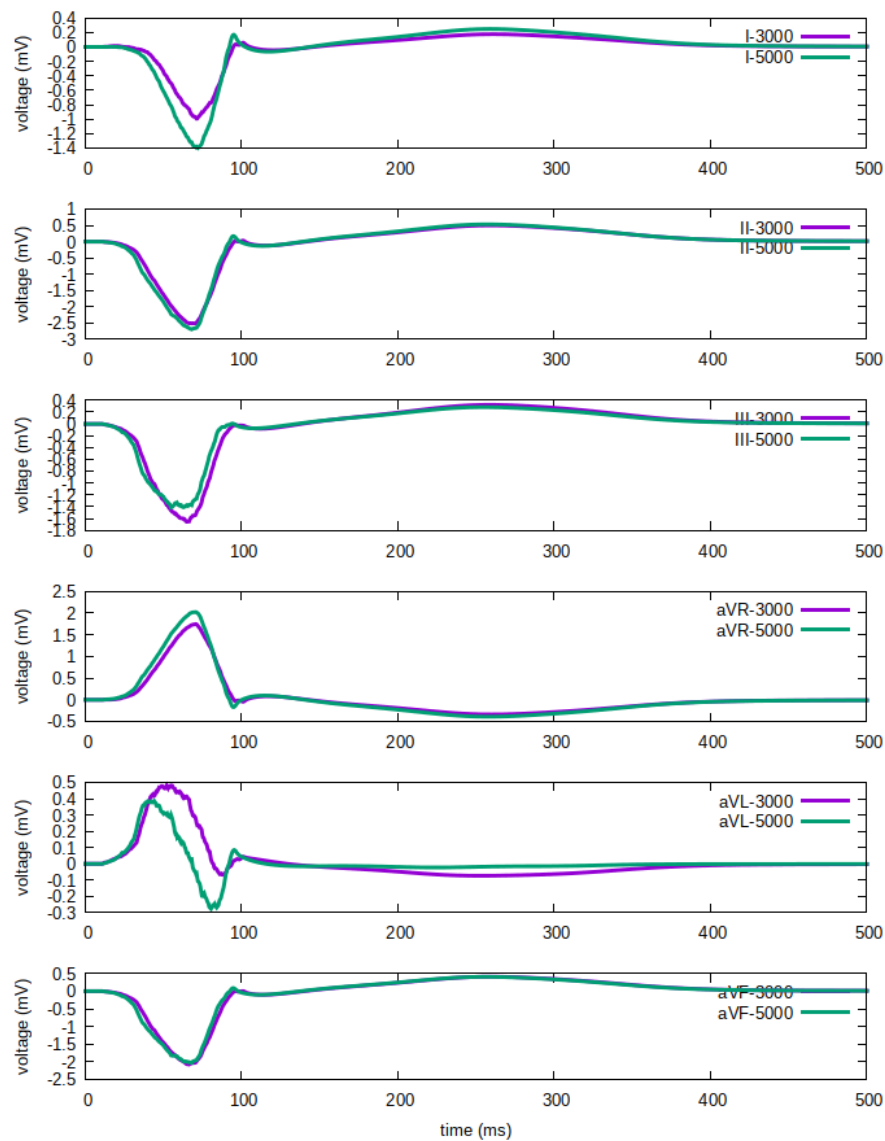


Figure 5.9: Limb leads ECG measurements of meshes with different resampling rates. Purple line is for the mesh resampled to a target mean edge length of  $3,000 \mu m$  and green line is for the mesh resampled to a target mean edge length of  $5,000 \mu m$ .

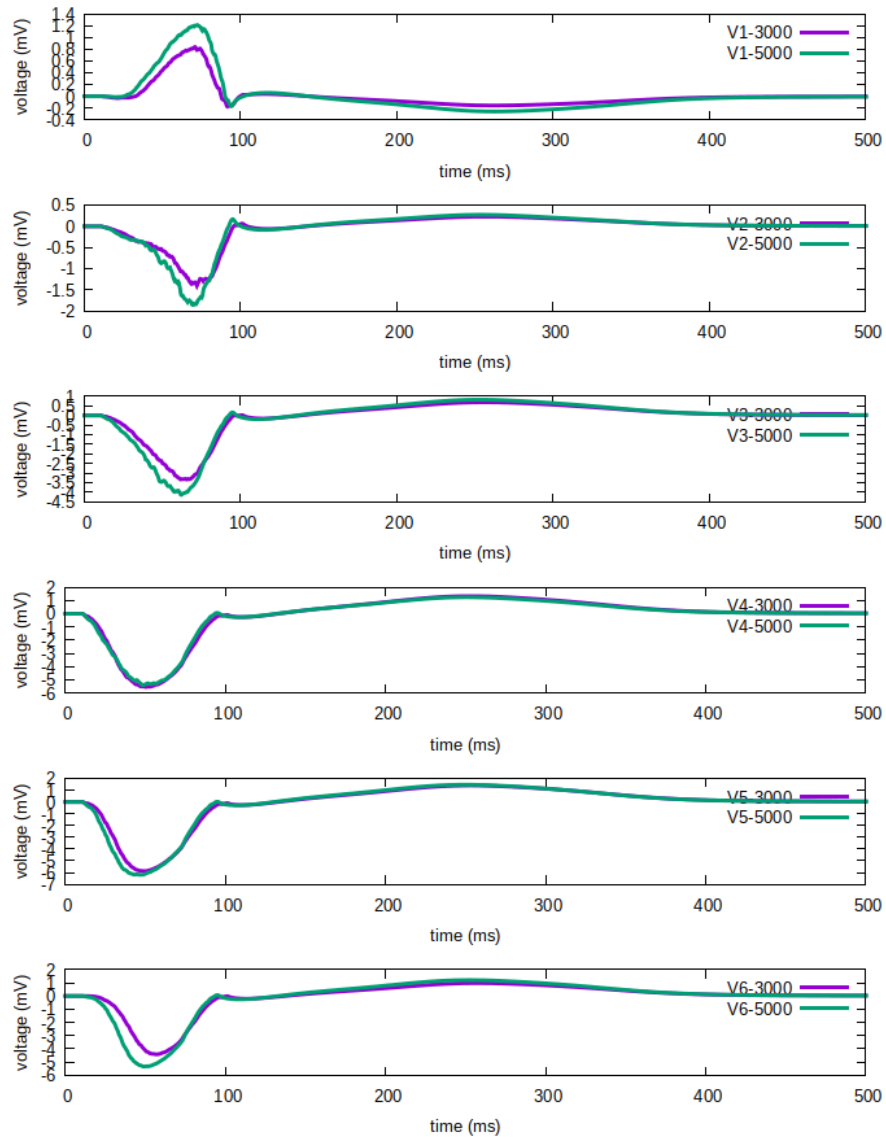


Figure 5.10: Chest leads ECG measurements of meshes with different resampling rates. Purple line is for the mesh resampled to a target mean edge length of 3,000  $\mu m$  and green line is for the mesh resampled to a target mean edge length of 5,000  $\mu m$ .

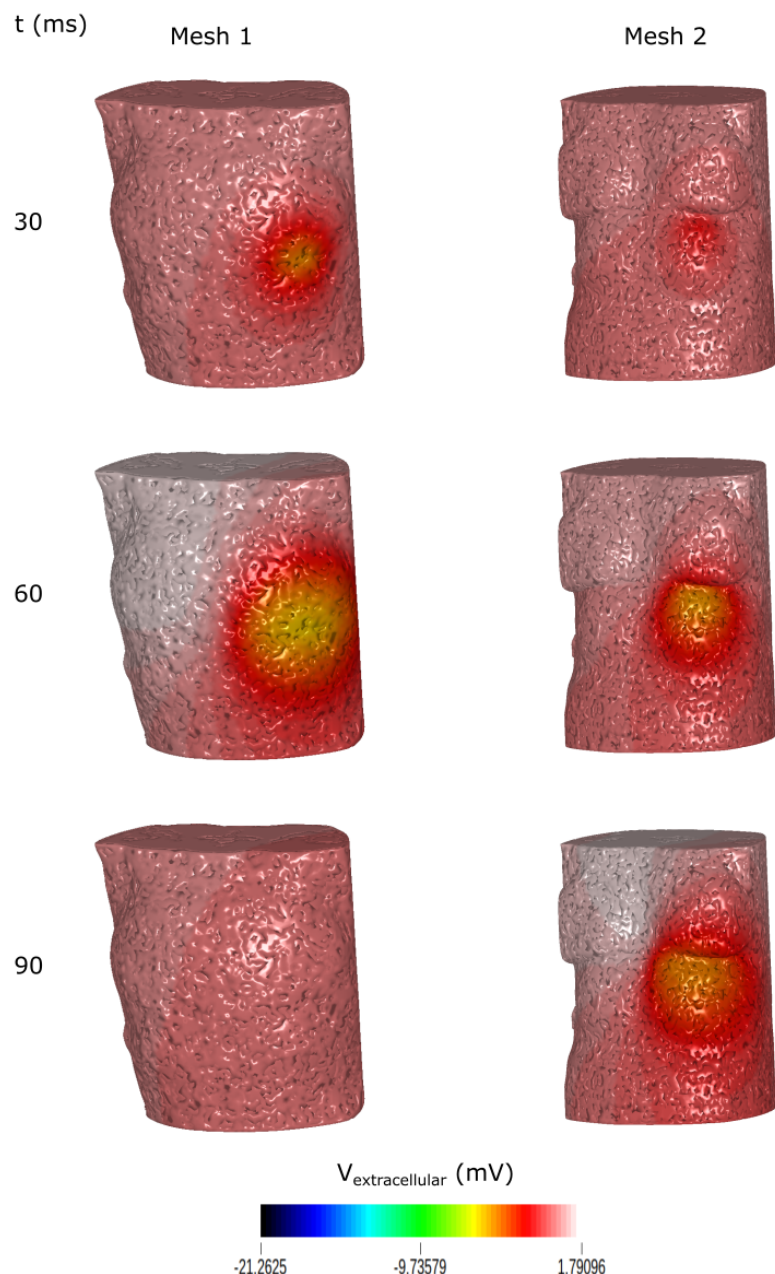


Figure 5.11: Extracellular potentials of the torso simulated with different mesh structures

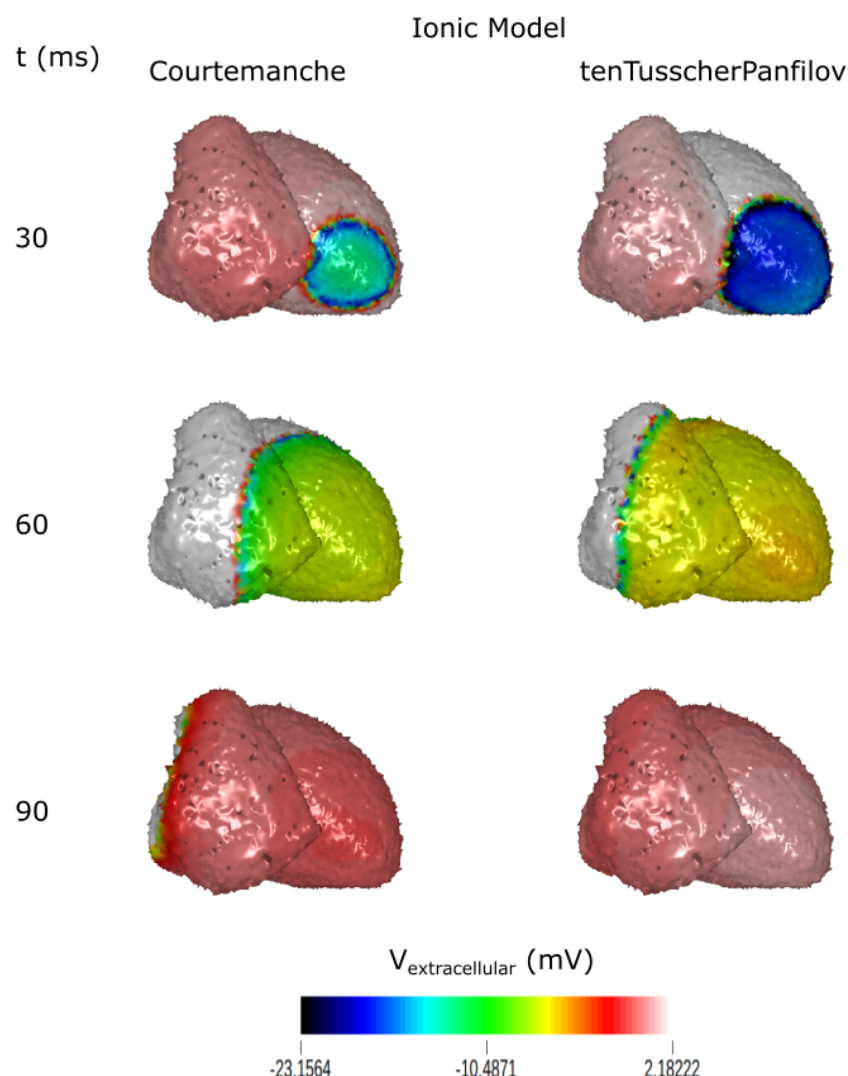


Figure 5.12: Extracellular potentials of the heart simulated with different ionic models

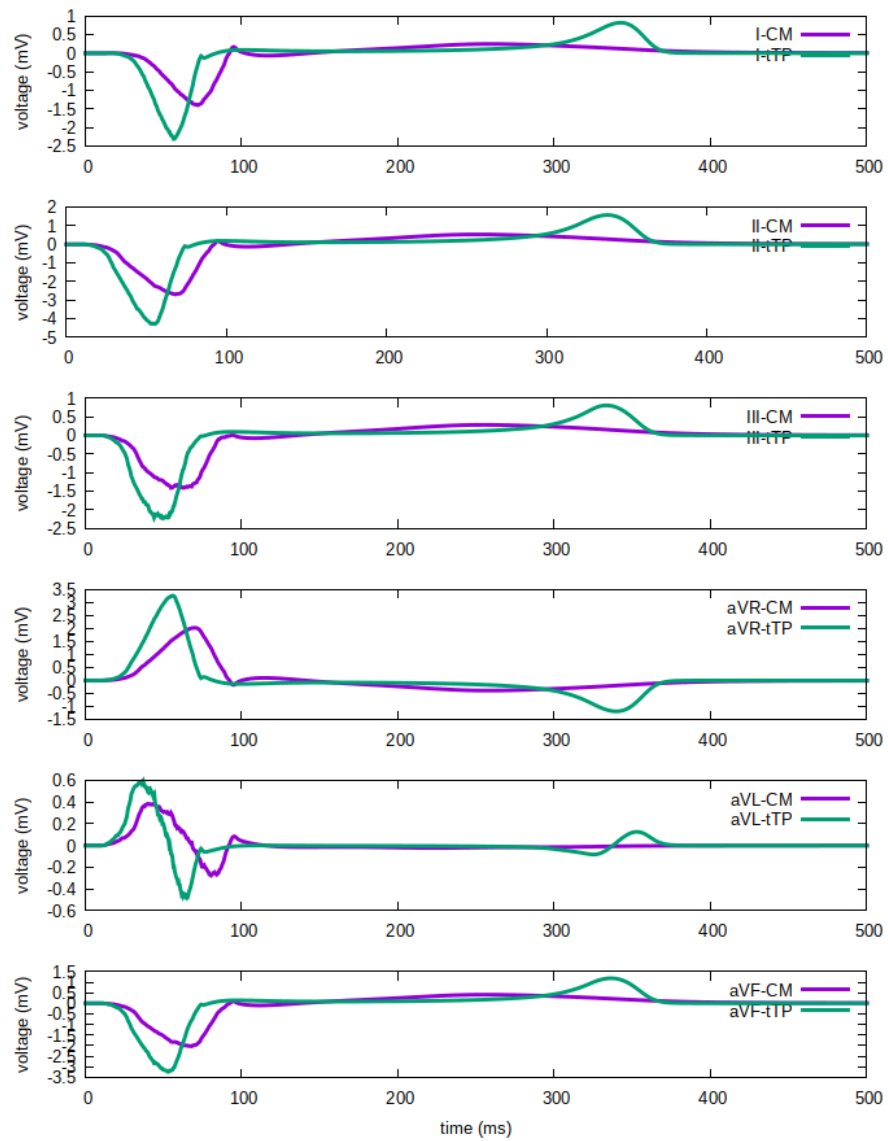


Figure 5.13: Limb leads ECG measurements of meshes with different ionic models. Purple line is for the simulation with the Courtemanche ionic model and green line is for the simulation with the tenTusscherPanfilov ionic model.

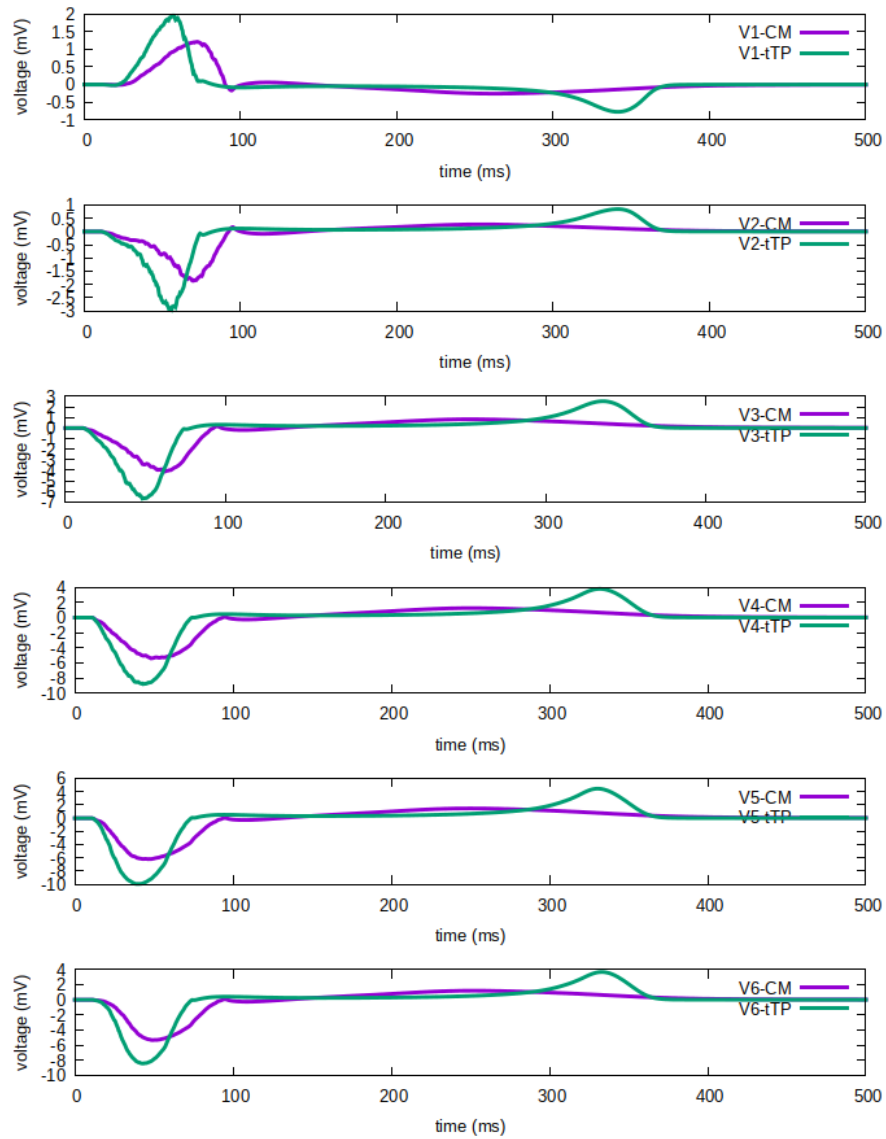


Figure 5.14: Chest leads ECG measurements of meshes with different ionic models. Purple line is for the simulation with the Courtemanche ionic model and green line is for the simulation with the tenTusscherPanfilov ionic model.

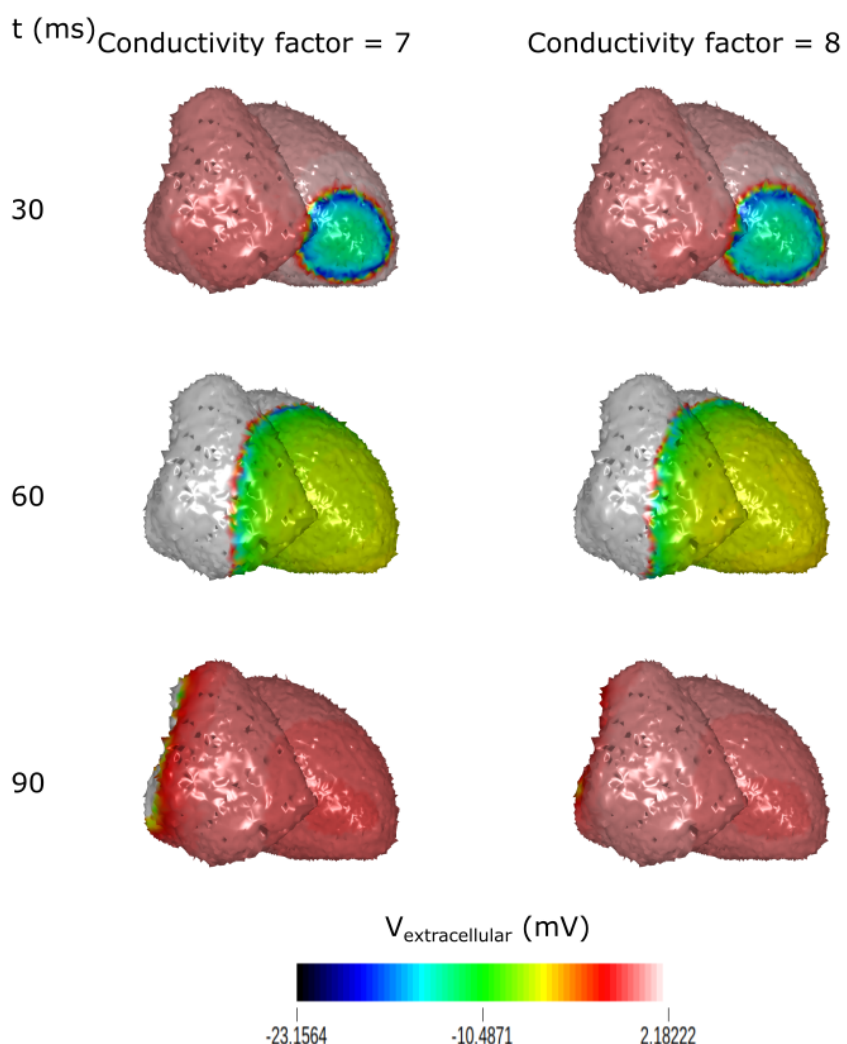


Figure 5.15: Extracellular potentials of the heart simulated with different conductivity factors

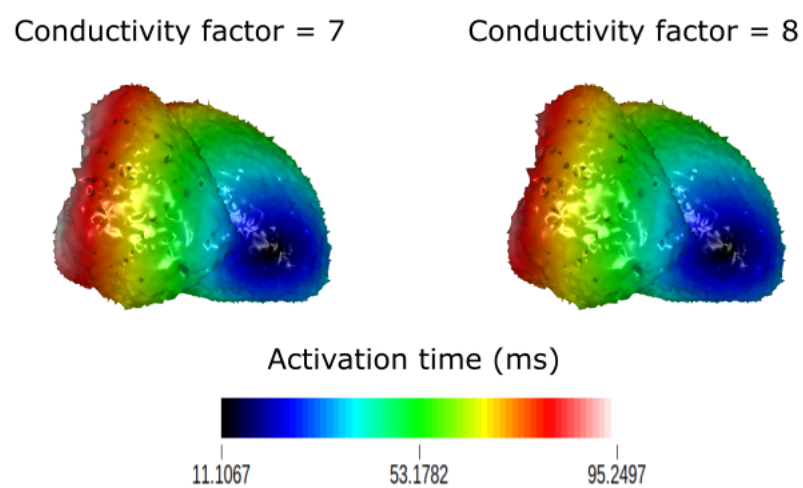


Figure 5.16: AT maps of the heart simulated with different conductivity factors

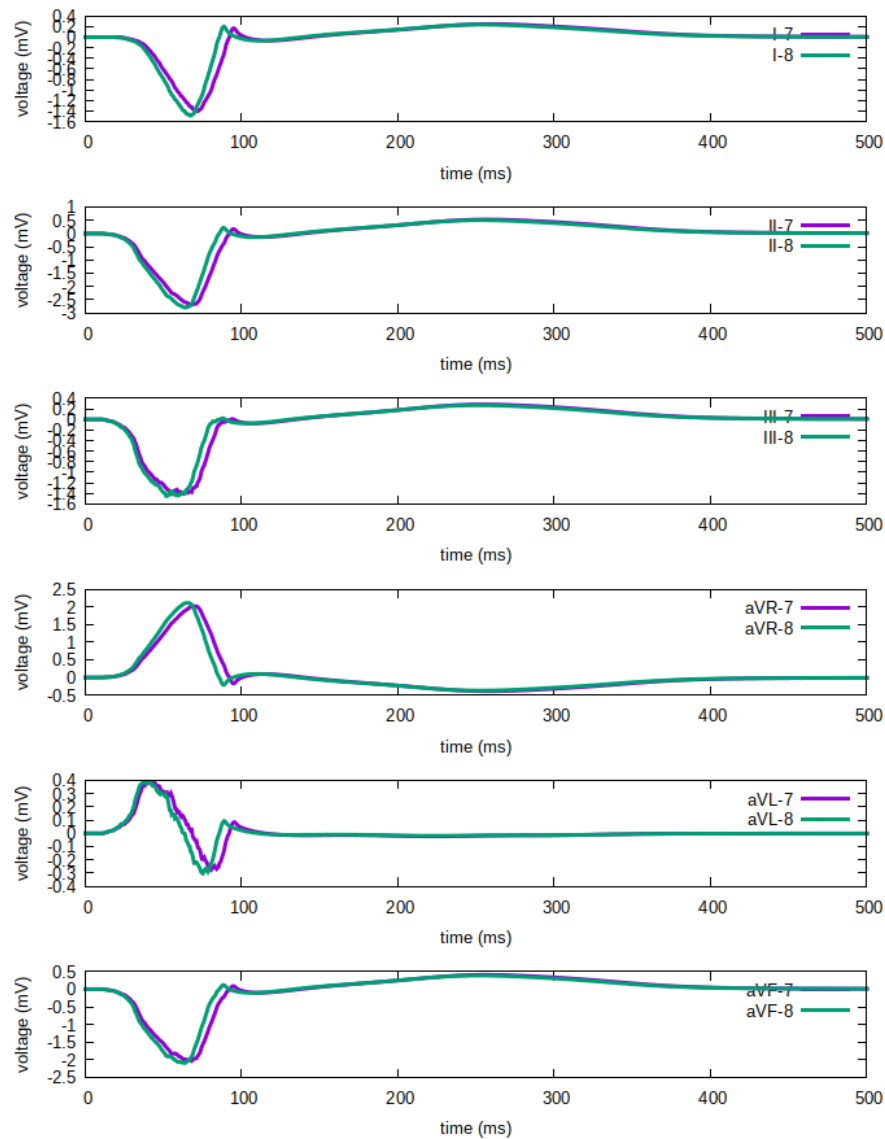


Figure 5.17: Limb leads ECG measurements of meshes with different conductivity factors. Purple line is for the simulation with conductivity factor of 7 and green line is for the simulation with conductivity factor of 8.

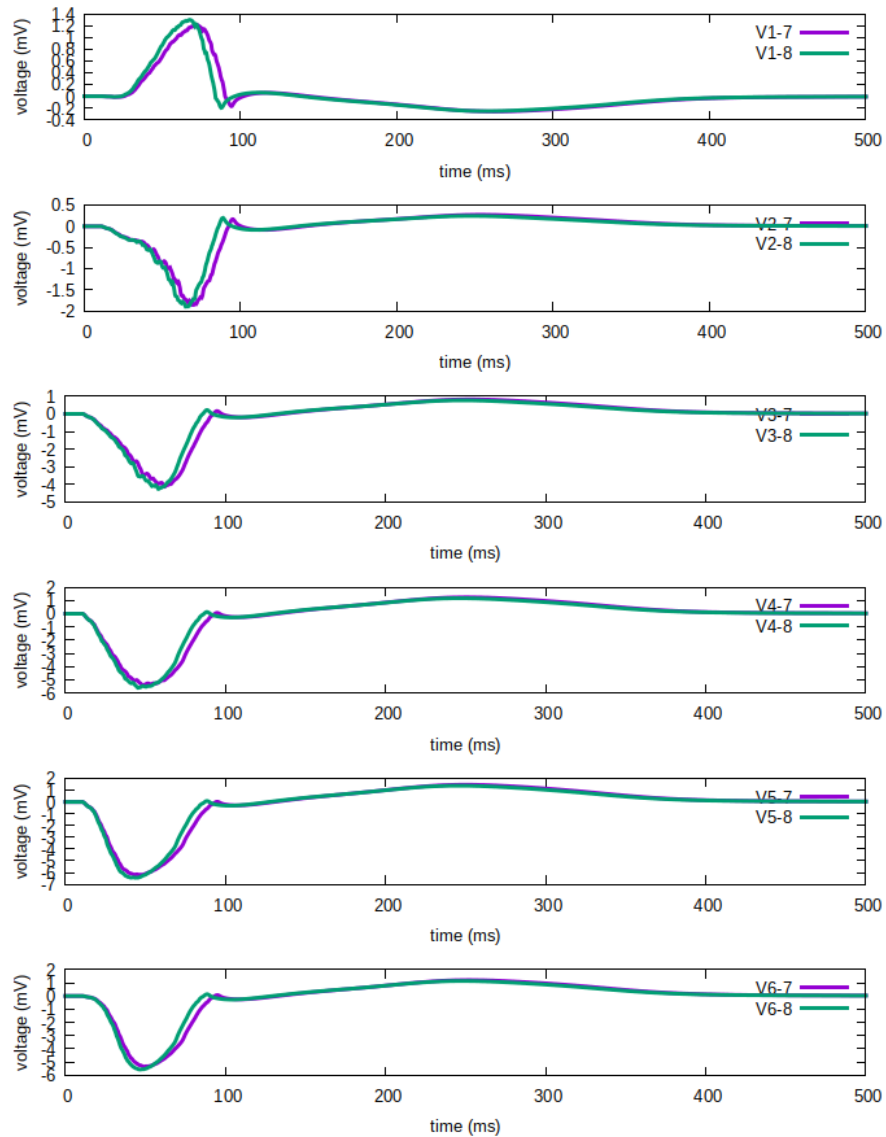


Figure 5.18: Chest leads ECG measurements of meshes with different conductivity factors. Purple line is for the simulation with conductivity factor of 7 and green line is for the simulation with conductivity factor of 8.

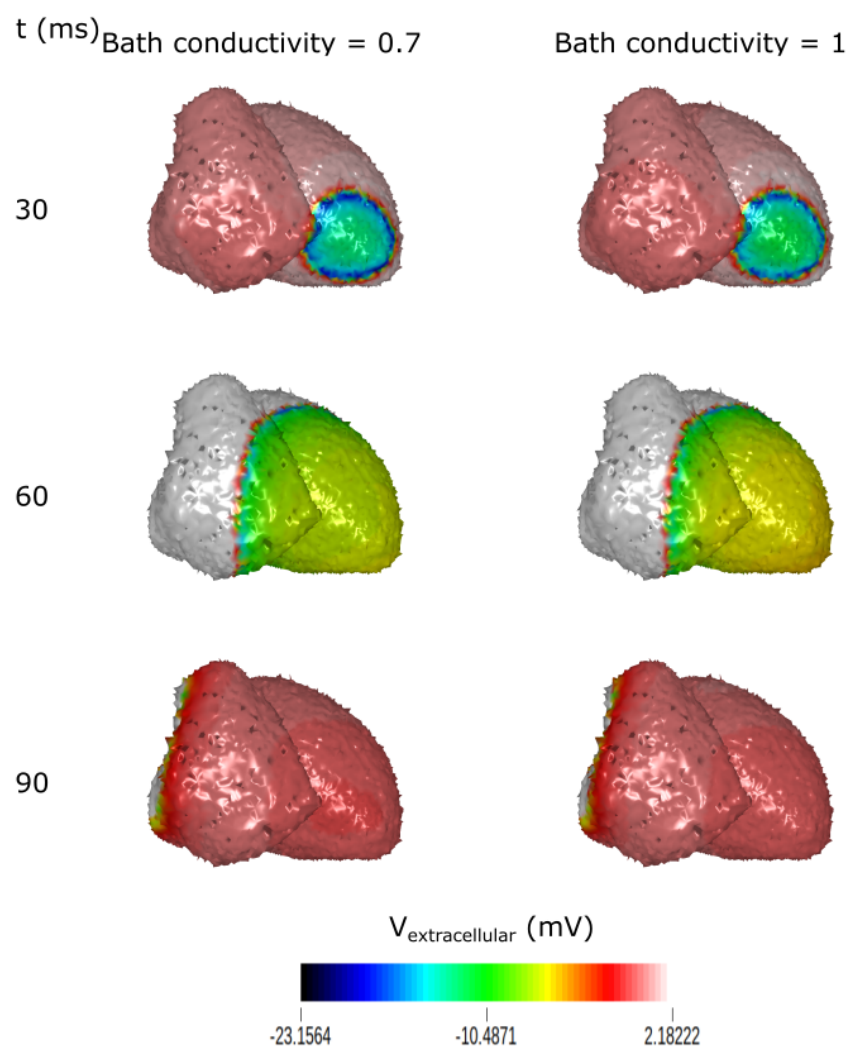


Figure 5.19: Extracellular potentials of the heart simulated with different bath conductivities

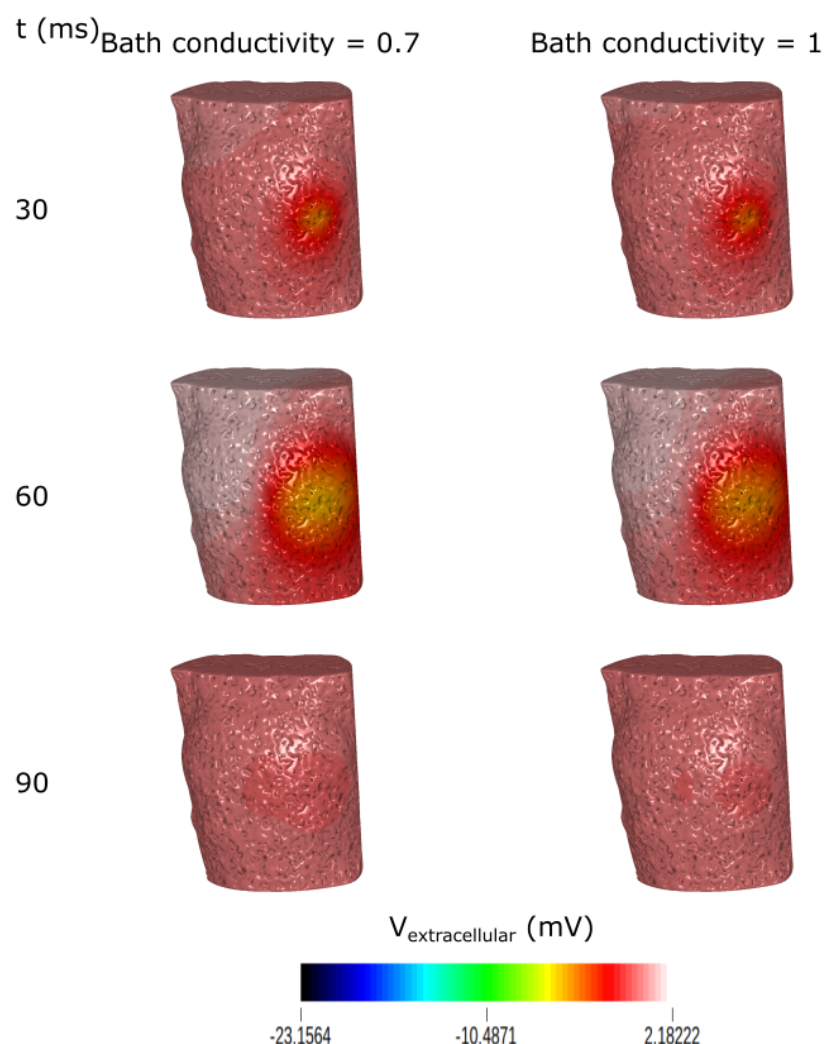


Figure 5.20: Extracellular potentials of the torso simulated with different bath conductivities

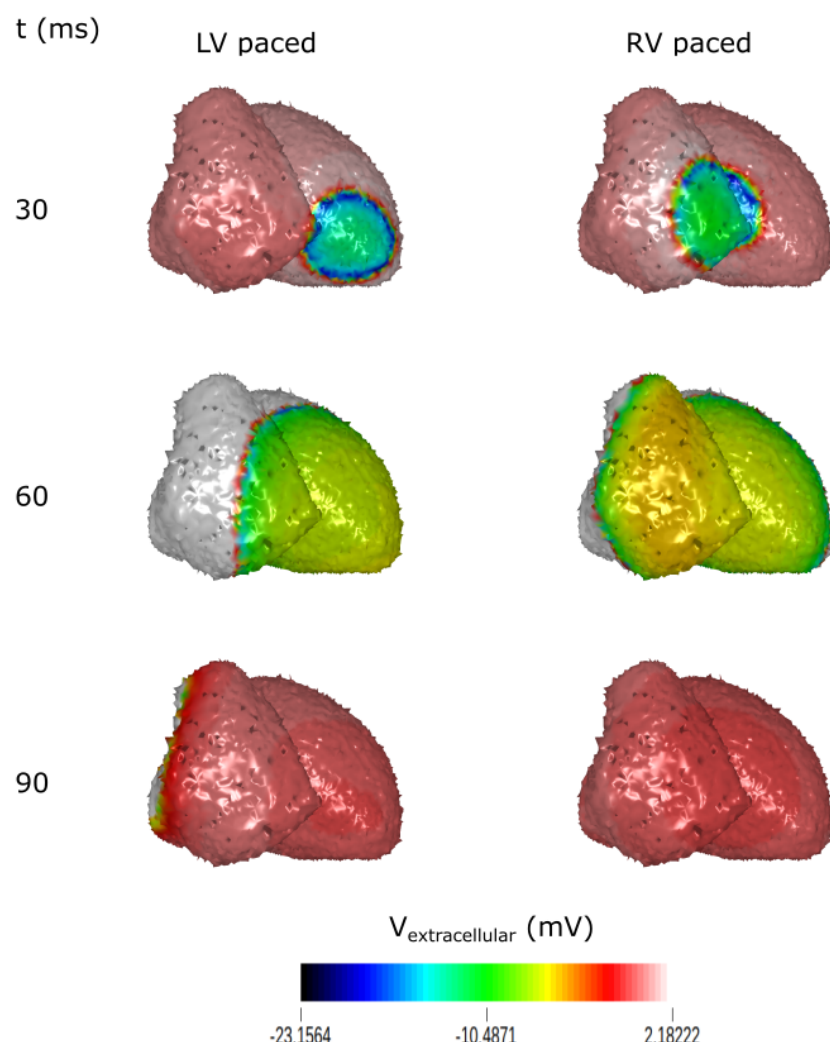


Figure 5.21: Extracellular potentials of the heart simulated from different stimulation points

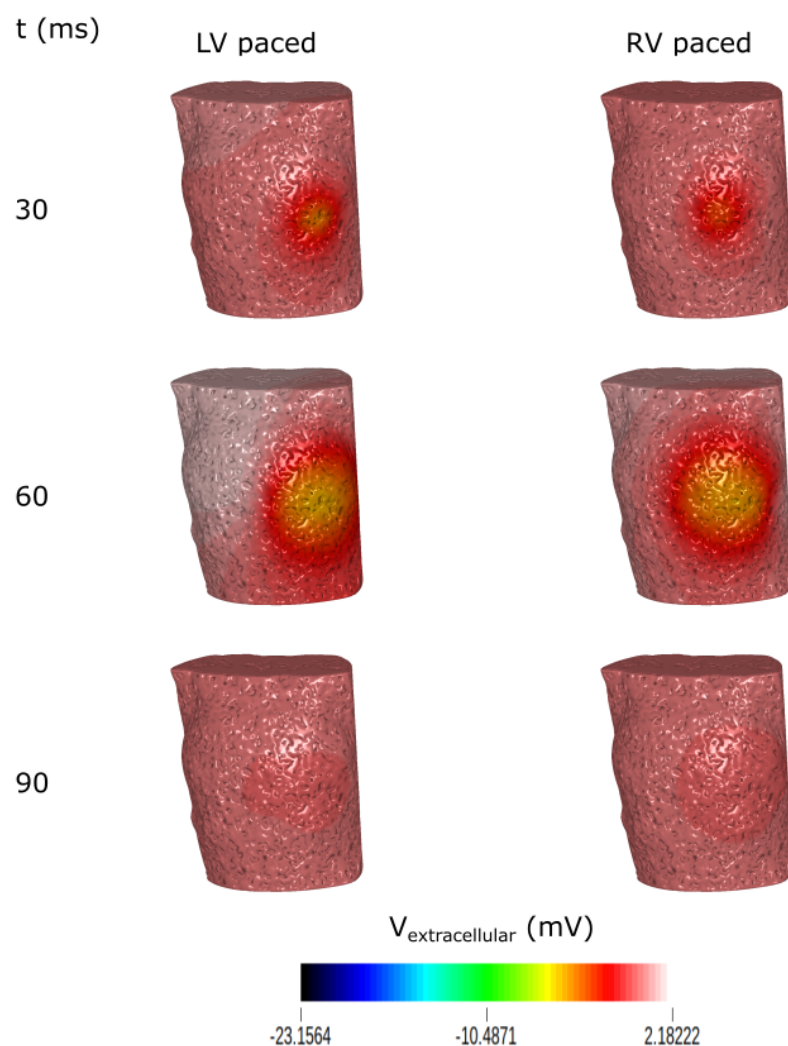


Figure 5.22: Extracellular potentials of the torso simulated from different stimulation points

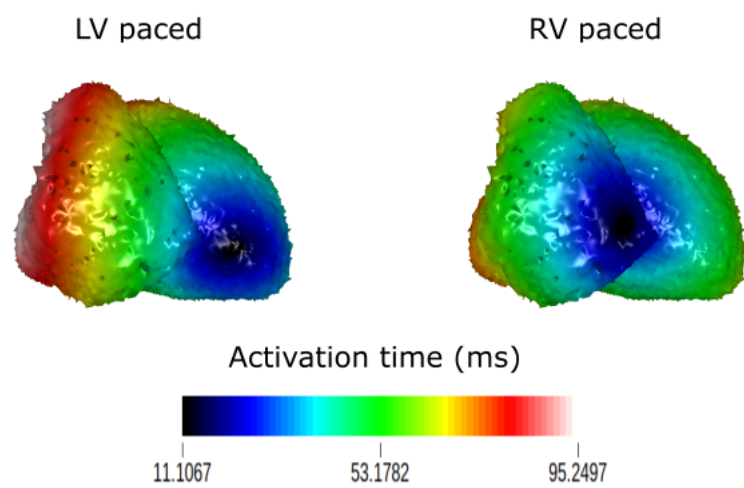


Figure 5.23: AT maps of the heart simulated from different stimulation points

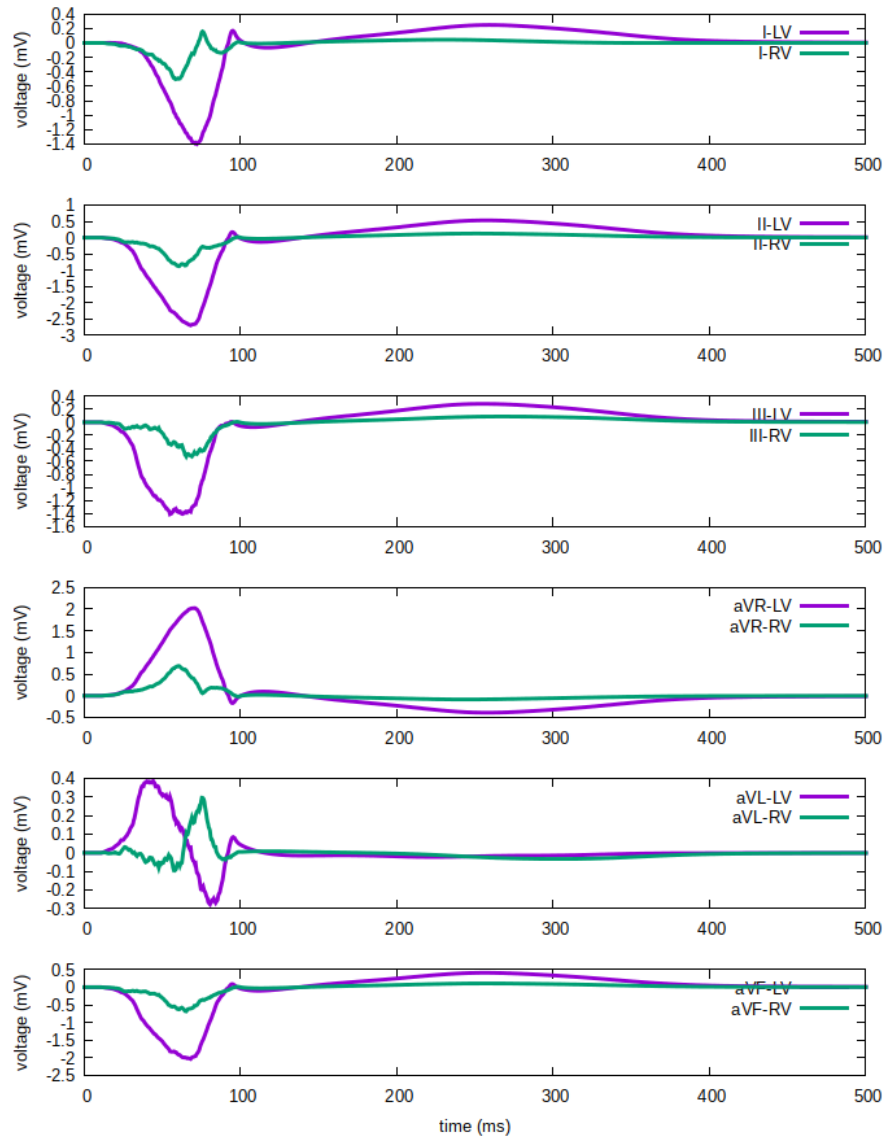


Figure 5.24: Limb leads ECG measurements of meshes with different stimulation points. Purple line is for the simulations stimulated from the left ventricle and green line is for the simulations stimulated from the right ventricle.

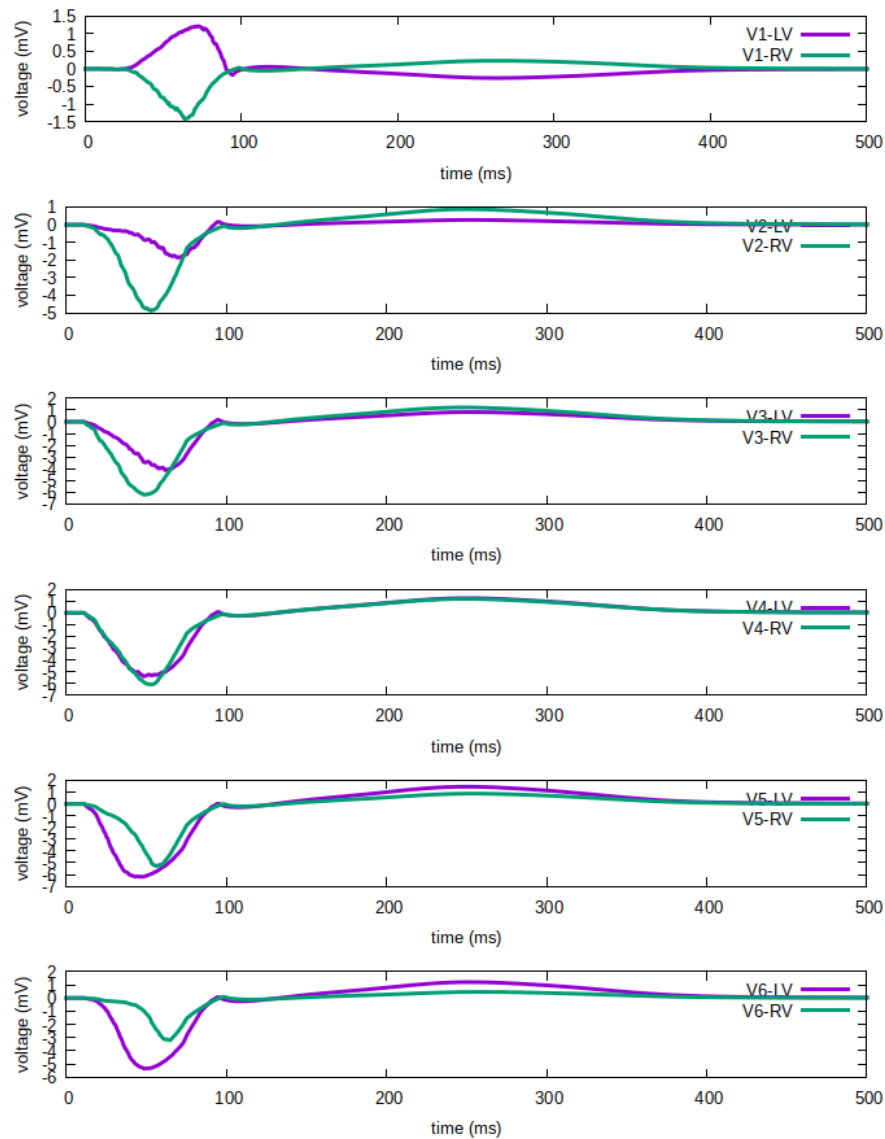


Figure 5.25: Chest leads ECG measurements of meshes with different stimulation points. Purple line is for the simulations stimulated from the left ventricle and green line is for the simulations stimulated from the right ventricle.

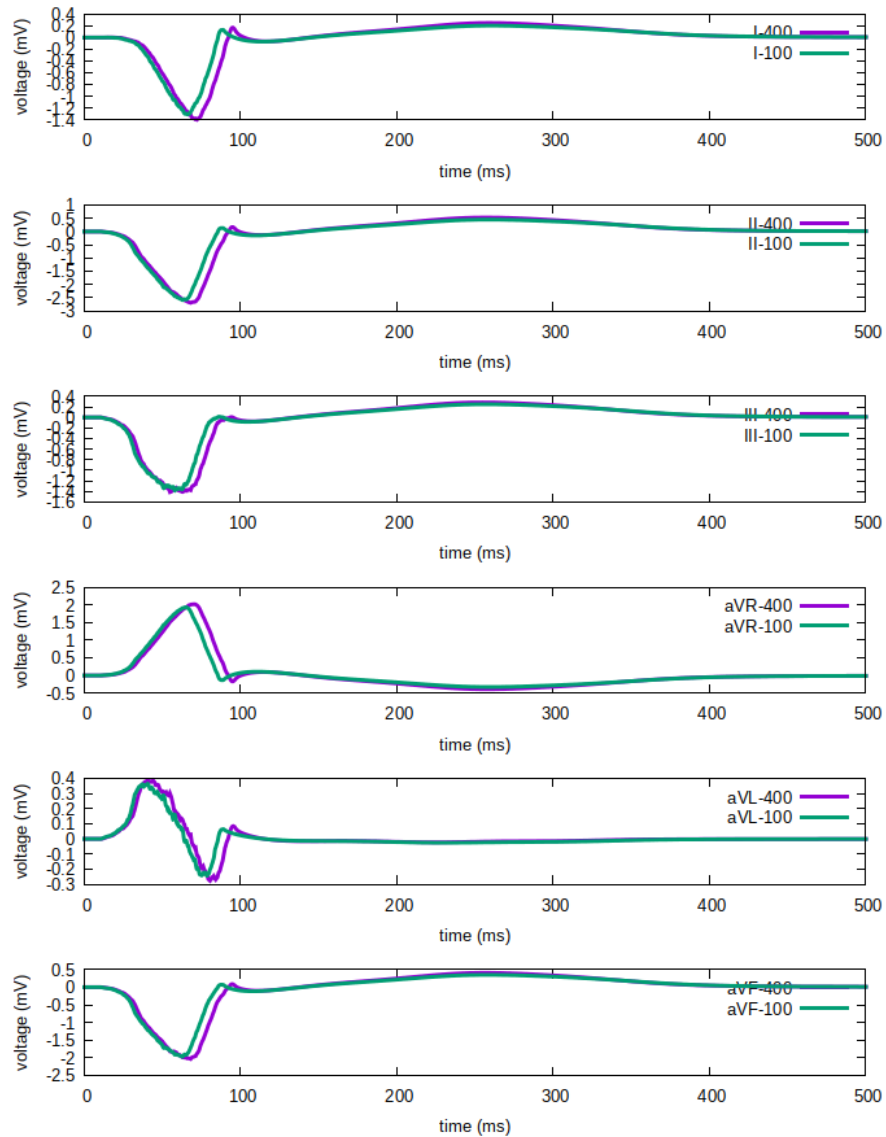


Figure 5.26: Limb leads ECG measurements of meshes with different time steps. Purple line is for the simulations run with a time step of  $400 \mu\text{s}$  and green line is for the simulations run with a time step of  $100 \mu\text{s}$ .

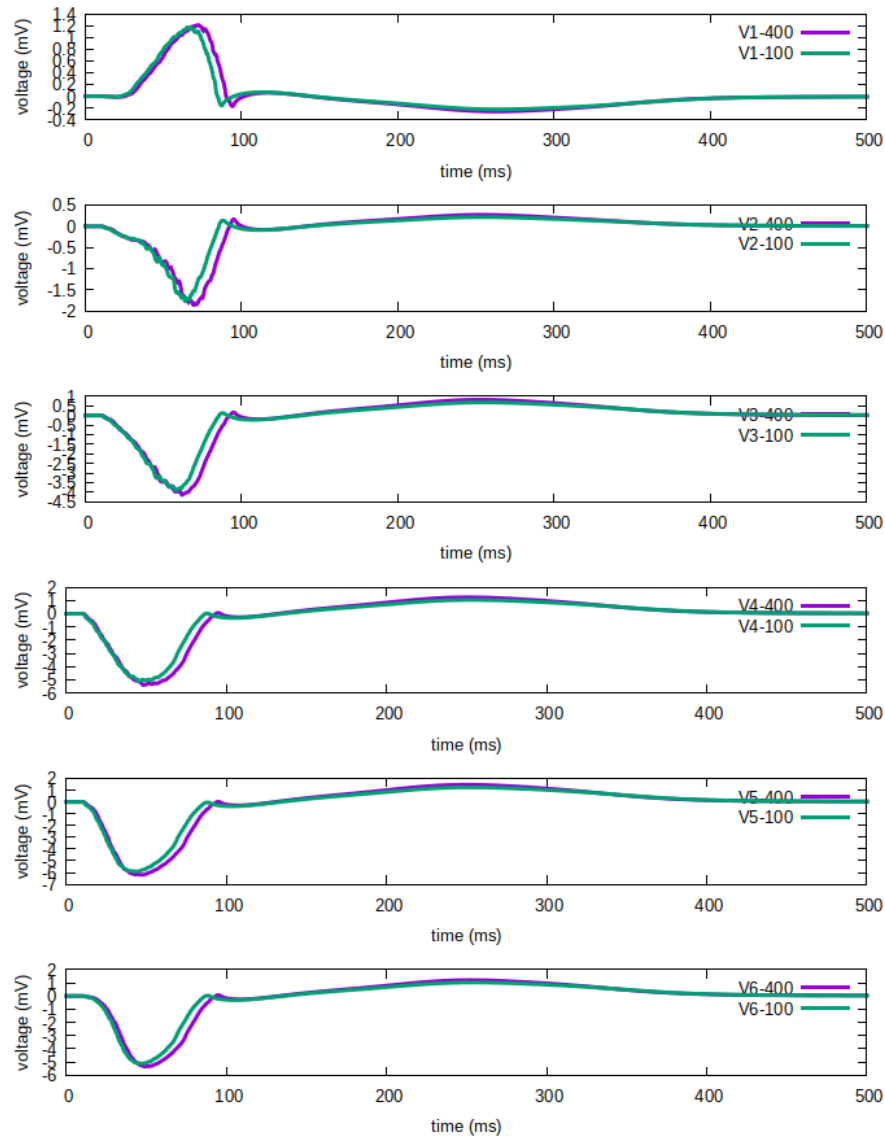


Figure 5.27: Chest leads ECG measurements of meshes with different time steps. Purple line is for the simulations run with a time step of  $400 \mu\text{s}$  and green line is for the simulations run with a time step of  $100 \mu\text{s}$ .

## 6 | Discussion

The objective of this study was to discover the key considerations and challenges in developing a simulation framework for modeling the electrophysiological activity of a beating heart. This exploration was planned to be guided by the performance assessment of this framework in generating 12-lead ECG signals. The outcomes of this study were expected to result in a pipeline that is capable of simulating 12-lead ECG patterns belonging to various pathologies and physiological features. Later on, the simulated ECG patterns having an immense diversity are projected to be included in the training and testing of data-intensive machine learning-based algorithms.

Choosing the CEP simulation environment as openCARP, various simulation settings were experimented and their impact on 12-lead ECG generation has been evaluated through extracellular potential maps on heart and torso surface along with AT maps and 12-lead ECG measurements. The source model, resampling rate, mesh structure, ionic model, conductivity coefficients, stimulus location, and the time step to solve numeric equations are found to be the key players in simulation framework development. The specifics of these consideration points are discussed in this chapter exhaustively.

The correct choice of the source model is elementary as it allows for the incorporation of bath loading effects or the recovery of torso extracellular potentials, all while addressing computational considerations. Running the experiment using the same mesh it was only possible to compare transmembrane potentials on epicardial surface between various source models since the monodomain model does not intrinsically generate torso and heart extracellular potentials. Although it is still realizable to obtain ECG measurements through recovery techniques, the monodomain model is not recommended for 12-lead ECG simulations due to its presumption of equally anisotropic intracellular and extracellular spaces[23, 27]. On the other hand, as can be seen in Table 5.1 there are drastic differences in computation duration between these models. Nevertheless, sticking with the literature, bidomain model is preferred in this work for the generation of the most realistic ECG signals[26].

In the hospital, the anatomy of the patient has an inevitable effect on the morphology of the ECG signal[93]. Therefore, the inclusion of different geometries is warranted. Moreover, the dense mesh structures are subject to resampling for an extensive ECG simulation study. The resampling and thereby the quality of the meshes are key contributors to the selection of many other attributes of the sim-

ulation framework. Bearing all of these in mind, the performance of the pipeline is assessed resulting in Table 5.2. Radical improvements in computation duration are observed as the mean edge length is increased. It is noteworthy that the target mean edge length is not achieved by Meshtool due to quality considerations of the resampling algorithm[83]. Despite the apparent decrease in smoothness of the torso, extracellular potentials are found to be almost identical along with the ECG signals as shown in Figures 5.8, 5.9, and 5.10 between meshes having a mean edge length of 4895 and 6580  $\mu\text{m}$ . In contrast, having two completely different subject torso meshes demands setting adjustments such as conductivity factor and results in completely different ECG patterns.

The CEP modelling framework requires an ionic model for the mathematical formulation of the ionic currents relating them to the membrane potentials. These models are subject to modifications introducing the effects of pathologies and induced drugs through alterations of ion channel equations[9, 55]. However, such manipulations are beyond the scope of this thesis. Regardless, two different ionic models, namely Courtemanche and tenTusscherPanfilov, are included in the pipeline, giving potential for such manipulations in further studies.

Scaling of conductivity tensors is found to be vital for simulations to converge. When these tensors are not scaled with the correct factor, simulations tend to diverge and thereby crash at random points. The iterative approach allowed correct conductivity factors to be found while still relying on previously reported coefficients[89]. The leading and lagging patterns belonging to different conductivity factors are seen clearly on epicardial surface and ECG leads in Figures 5.15, 5.16, 5.17, and 5.18. In contrast, bath conductivity changes showed indistinguishable patterns on the torso surface as well as ECG leads.

The initiation of electrical activity of the heart is purely dependent on the choice of the stimulation point. Due to the fact that only ventricle fiber structures are available for this study, stimulation points were chosen on the epicardial surface between the septum and apex of the heart as they are found to be one of the most sensitive stimulation nodes[63]. The pacing is done from the left and right ventricles reanimating the initiation of the ventricle contractions. The resulting ECG pattern is not typical of the QRS complex mainly due to the atria structure being absent. However, the comparison of it with similar experiments from the PhysioNet database, specifically the one from the study of Kalyakulina et al. showed similar patterns[94, 95].

The proposed framework in this study is subject to restrictions. Mainly, atria fiber orientations not being available prevents us from generating the complete ECG pattern. However, the literature review indicates that ECG simulation studies usually focus on only atria or ventricles to observe the P wave or QRST complex, respectively[55]. Moreover, the torso geometry must be available for the proposed pipeline since the bidomain source model is chosen for ECG simulations. Consequently, as in many different studies of biomedical engineering, the availability of anatomical structures has a vital role in our study.

The number of stimulus points being limited to only one node is another hindering

factor of this study. For the realistic activation of the ventricles most of the PMJs must be stimulated synchronously warranting several stimuli located in anatomically precise positions[63]. In a case where atria fibers are available SA and AV nodes must be modeled while a layer modeling the intricate dynamics between atria and ventricles is generated. Moreover, the selection of lead locations must be tailored to the patient’s anatomy, considering the torso mesh structure provided. In addition, clinical ECG recordings would augment the evaluation of the realism of the 12-lead ECG signals generated by the proposed pipeline.

The CEP simulation framework development is an extensive task involving the decision of numerous models and relevant parameters. The range of this work was strictly limited both in terms of the diversity of simulation parameters and available mesh sources. Furthermore, computational sources are limited allowing only a certain number of simulations to be run in the time interval of this thesis. Nevertheless, a robust pipeline enabling realistic ECG simulations has been developed.

Having a framework with the capacity of realistic ECG generation provides great potential for future experiments. Besides, further evaluation metrics can be introduced and the performance of the pipeline can be challenged with clinical ECG data. Here we list the pivotal improvements that can be made to expand the functionality of the proposed framework:

- Incorporation of the atria could enable the complete construction of the ECG pattern. However, the atria fiber orientations must also be accounted for. This could be done by the rule-based approach[81]. Furthermore, realistic simulations would require an electrical isolation between the atria and the ventricles. In such a case, the AV node must be modeled as in the study of Gilette et al.[78].
- Number of stimulus locations could be increased for a better representation of PMJs and thereby ventricle contractions.
- openCARP can be built on supercomputers. The availability of more computing power could discard resampling and thereby caused conductivity scaling need. This would increase the precision of the ECG generation.
- The clinical data obtained from the same anatomy that is being used in simulations could provide a ground truth for the evaluation of ECG patterns.
- Further diversifying parameters explored in this study could provide a training data having great variation appropriate for data-intensive machine learning-based algorithms.
- Through modifications of the parameters specific pathologies and induction of drugs could be studied.
- The sensitivity of ECGs related to the lead positions could be analyzed by Monte Carlo sampling.

## 7 | Conclusion

In this study, the foundation of a pipeline to generate 12-lead ECG signals from a beating heart was outlined. During the process, intricacies of developing a simulation framework for modeling the cardiac electrophysiological activity were explored. The resultant framework ended up having the potential to be expanded to a complete healthy heart 12-lead ECG simulator. Nonetheless, already implemented framework is capable of generating realistic ECG patterns for specific settings.

The key components for 12-lead ECG simulations are found to be the source model, mesh properties, region specifications, stimulus definition, and simulator options. All of these were modified within the chosen simulation environment and emerging ECG signals were assessed thoroughly. Moreover, further visualization aids were facilitated to give deeper insights into electrical potential distributions and ATs. Correlation coefficients with a base model were also presented to provide a quantitative metric showing how strong the effect of a setting change is.

The limitations of this study were clearly delineated. The lack of atria fiber structures along with the limited number of stimuli points were the main setbacks of this study. Moreover, the absence of clinical ECG data belonging to the patient whose torso structure was used impaired the evaluation validity. Nevertheless, the establishment of the framework was given in great detail accompanied by code excerpts thereby enabling the reader to reproduce the pipeline and results. Furthermore, pivotal improvement points were listed giving a concrete perspective on future work.

To sum it all up, in this thesis, key considerations and challenges in developing a simulation framework for modeling the electrical activity of a beating heart were explored and analyzed through the implementation of a pipeline performing the task of generating 12-lead ECG signals.

## 8 | Bibliography

- [1] Gregory A Roth, Catherine Johnson, Amanuel Abajobir, Foad Abd-Allah, Semaw Ferede Abera, Gebre Yitayih Abyu, Muktar Ahmed, Baran Aksut, Tahiya Alam, Khurshid Alam, François Alla, Nelson Alvis-Guzman, Stephen Amrock, Hossein Ansari, Johan Ärnlöv, Hamid Asayesh, Tesfay Mebrahtu Atey, Leticia Avila-Burgos, Ashish Awasthi, Amitava Banerjee, Aleksandra Barac, Till Bärnighausen, Lars Barregard, Neeraj Bedi, Enyew Belay Ketema, Derrick Bennett, Kidanemariam Berhe, Zulfiqar Bhutta, Semaw Bitew, Jonathan Carapetis, Juan J Carrero, Deborah Carvalho Malta, Carlos A Castañeda-Orjuela, Jacqueline Castillo-Rivas, Ferrán Catalá-López, Jee-Young Choi, Hanne Christensen, Massimo Cirillo, Leslie Jr Cooper, Michael Criqui, David Cundiff, Albertino Damasceno, Lalit Dandona, Rakhi Dandona, Kairat Davletov, Samath D Dharmaratne, Prabhakaran Dorairaj, Manisha Dubey, Rebecca Ehrenkranz, Maysaa El Sayed Zaki, Emerito Jose A Faraon, Alireza Esteghamati, Talha Farid, Maryam Farvid, Valery Feigin, Eric L Ding, F Gerry R Fowkes, Tsegaye Gebrehiwot, Richard Gillum, Audra Gold, Philimon Gona, Rajeev Gupta, Tesfaye Desta Habtewold, Nima Hafezi-Nejad, Gessessew Bugssa Hailu, Alemayehu Desalegne Hailu, Graeme Hankey, Hamid Yimam Hassen, Kalkidan Hassen Abate, Rasmus Havmoeller, Simon I Hay, Masako Horino, Peter J Hotez, Kathryn Jacobsen, Spencer James, Mehdi Javanbakht, Pan niyammakal Jeemon, Denny John, Jost B Jonas, Yogeshwar Kalkonde, Chante Karimkhani, Amir Kasaeian, Yousef Saleh Khader, Abdur Rahman Khan, Young-Ho Khang, Sahil Khera, Abdullah T Khoja, Jagdish Khubchandani, Daniel Kim, Dhaval Kolte, Soewarta Kosen, Kristopher J Krohn, G Anil Kumar, Gene F Kwan, Dharmesh K Lal, Anders Larsson, Shai Linn, Alan Lopez, Paulo A Lotufo, Hassan Magdy Abd El Razek, Reza Malekzadeh, Mohsen Mazidi, Toni Meier, Kidanu Gebremariam Meles, George Mensah, Atte Mero toja, Haftay Berhane Mezgebe, Ted Miller, Erkin Mirrakhimov, Shafiu Mohammed, Andrew E Moran, Kamarul Imran Musa, Jagat Narula, Bruce Neal, Frida N Ngalesoni, Grant Nguyen, Carla M Obermeyer, Mayowa Owolabi, George Patton, João Pedro, Dima Qato, Mostafa Qorbani, Kazem Rahimi, Rajesh Kumar Rai, Salman Rawaf, Antonio L Ribeiro, Saeid Safiri, Joshua A Salomon, Itamar Santos, Milena Santric Milicevic, Benn Sartorius, Aletta Schutte, Sadaf Sepanlou, Masood Ali Shaikh, Min-Jeong Shin, Mehdi Shishehbor, Hirsh Shore, Diego Augusto Santos Silva, Eugene Sobngwi, Saverio Stranges, Soumya

- Swaminathan, Rafael Tabarés-Seisdedos, Niguse Tadele Atnafu, Fisaha Haile Tesfay, J S Thakur, Amanda Thrift, Roman Topor-Madry, Thomas Truelsen, Stefanos Tyrovolas, Kingsley Nnanna Ukwaja, Olalekan Uthman, Tommi Vasankari, Vasiliy Vlassov, Stein Emil Vollset, Tolassa Wakayo, David Watkins, Robert Weintraub, Andrea Werdecker, Ronny Westerman, Charles S Wiysonge, Charles Wolfe, Abdulhalik Workicho, Gelin Xu, Yuichiro Yano, Paul Yip, Nao-hiro Yonemoto, Mustafa Younis, Chuanhua Yu, Theo Vos, Mohsen Naghavi, and Christopher Murray. Global, regional, and national burden of cardiovascular diseases for 10 causes, 1990 to 2015. *J Am Coll Cardiol*, 70:1–25, 7 2017.
- [2] Xiaoye Zhao, Jucheng Zhang, Yinglan Gong, Lihua Xu, Haipeng Liu, Shujun Wei, Yuan Wu, Ganhua Cha, Haicheng Wei, Jiandong Mao, and Ling Xia. Reliable detection of myocardial ischemia using machine learning based on temporal-spatial characteristics of electrocardiogram and vectorcardiogram. *Frontiers in Physiology*, 13, 5 2022.
  - [3] Richard E Klabunde. Cardiac electrophysiology: normal and ischemic ionic currents and the ecg. *Adv Physiol Educ*, 41:29–37, 2017.
  - [4] Dipal Savla Desai and Samer Hajouli. Arrhythmias, 6 2023. [Updated 2023 Jun 5].
  - [5] Dennis M. Krikler. Historical aspects of electrocardiography. *Cardiology Clinics*, 5:349–355, 1987.
  - [6] W. Bruce Fye. A history of the origin, evolution and impact of electrocardiography. *The American Journal of Cardiology*, 73:937–949, 1994.
  - [7] Yasir Sattar and Lovy Chhabra. Electrocardiogram, 6 2023. [Updated 2023 Jun 5].
  - [8] Peter W Macfarlane, Adriaan Van Oosterom, Olle Pahlm, Paul Kligfield, Michiel Janse, and John Camm. *Comprehensive Electrocardiology*, volume 1. Springer, 2 edition, 2011.
  - [9] Steven A. Niederer, Joost Lumens, and Natalia A. Trayanova. Computational models in cardiology. *Nature Reviews Cardiology*, 16:100–111, 2 2019.
  - [10] Gernot Plank, Axel Loewe, Aurel Neic, Christoph Augustin, Yung Lin Huang, Matthias A.F. Gsell, Elias Karabelas, Mark Nothstein, Anton J. Prassl, Jorge Sánchez, Gunnar Seemann, and Edward J. Vigmond. The opencarp simulation environment for cardiac electrophysiology. *Computer Methods and Programs in Biomedicine*, 208, 9 2021.
  - [11] W. Einthoven. Ueber die form des menschlichen electrocardiogramms. *Pflüger, Archiv für die Gesammte Physiologie des Menschen und der Thiere*, 60:101–123, 3 1895.

- [12] G. Ling and R. W. Gerard. The normal membrane potential of frog sartorius fibers. *Journal of cellular physiology*, 34:383–396, 12 1949.
- [13] Erwin Neher, Bert Sakmann, and Joe Henry Steinbach. The extracellular patch clamp: A method for resolving currents through individual open channels in biological membranes. *Pflugers Archiv European Journal of Physiology*, 375:219–228, 7 1978.
- [14] J Gordon Betts, Tyler Junior College, Peter Desaix, Jody E Johnson, James A Wise, Mark Womble, and Kelly A Young. *Anatomy & Physiology*. openstax, 2013.
- [15] Mark W Barnett, Philip M Larkman, M W Barnett, and P M Larkman. The action potential. *Pract Neurol*, 7:192–197, 2007.
- [16] Gary R. Skuse and Maureen C. Ferran. *Cardiomyocytes*, volume 1299. Springer New York, 2015.
- [17] A L Hodgkin and A F Huxley. A quantitative description of membrane current and its application to conduction and excitation in nerve. *J. Physiol*, pages 500–544, 1952.
- [18] Anthony H Kashou, Amit Goyal, Thao Nguyen, Intisar Ahmed, and Lovely Chhabra. Atrioventricular block, 2 2023. [Updated 2023 Feb 24]. In: StatPearls [Internet]. Treasure Island (FL): StatPearls Publishing; 2023 Jan-.
- [19] Leslie Tung. A bi-domain model for describing ischemic myocardial d-c potentials. 1978.
- [20] Piero Colli Franzone, Luca Franco Pavarino, and Simone Scacchi. *Mathematical Cardiac Electrophysiology*, volume 13. Springer International Publishing, 2014.
- [21] Alejandro Lopez-Perez, Rafael Sebastian, and Jose M. Ferrero. Three-dimensional cardiac computational modelling: methods, features and applications, 4 2015.
- [22] E. J. Vigmond, R. Weber dos Santos, A. J. Prassl, M. Deo, and G. Plank. Solvers for the cardiac bidomain equations. *Progress in Biophysics and Molecular Biology*, 96:3–18, 1 2008.
- [23] Claudia Nagel, Cristian Barrios Espinosa, Karli Gillette, Matthias A.F. Gsell, Jorge Sanchez, Gernot Plank, Olaf Dössel, and Axel Loewe. Comparison of propagation models and forward calculation methods on cellular, tissue and organ scale atrial electrophysiology. *IEEE Transactions on Biomedical Engineering*, 70:511–522, 2 2023.

- [24] Jean R. Bragard, Oscar Camara, Blas Echebarria, Luca Gerardo Giorda, Esther Pueyo, Javier Saiz, Rafael Sebastián, Eduardo Soudah, and Mariano Vázquez. Cardiac computational modelling. *Revista Española de Cardiología (English Edition)*, 74:65–71, 1 2021.
- [25] Mark Potse, Bruno Dubé, Alain Vinet, and René Cardinal. A comparison of monodomain and bidomain propagation models for the human heart. pages 3895–3898. Institute of Electrical and Electronics Engineers Inc., 2006.
- [26] Martin J. Bishop and Gernot Plank. Bidomain ecg simulations using an augmented monodomain model for the cardiac source. *IEEE Transactions on Biomedical Engineering*, 58:2297–2307, 8 2011.
- [27] Martin J. Bishop and Gernot Plank. Representing cardiac bidomain bath-loading effects by an augmented monodomain approach: Application to complex ventricular models. *IEEE Transactions on Biomedical Engineering*, 58:1066–1075, 4 2011.
- [28] James P Keener. An eikonal-curvature equation for action potential propagation in myocardium. *J. Math. Biol.*, 29:629–651, 1991.
- [29] Aurel Neic, Fernando O. Campos, Anton J. Prassl, Steven A. Niederer, Martin J. Bishop, Edward J. Vigmond, and Gernot Plank. Efficient computation of electrograms and ecgs in human whole heart simulations using a reaction-eikonal model. *Journal of Computational Physics*, 346:191–211, 10 2017.
- [30] Zhisong Fu, Robert M. Kirby, and Ross T. Whitaker. A fast iterative method for solving the eikonal equation on tetrahedral domains. *SIAM Journal on Scientific Computing*, 35, 2013.
- [31] Andrew J. Pullan, Karl A. Tomlinson, and Peter J. Hunter. A finite element method for an eikonal equation model of myocardial excitation wavefront propagation. *SIAM Journal on Applied Mathematics*, 63:324–350, 1 2002.
- [32] Yoram Rudy. The forward problem of electrocardiography revisited. *Circulation: Arrhythmia and Electrophysiology*, 8:526–528, 6 2015.
- [33] Brett M. Burton, Jess D. Tate, Burak Erem, Darrell J. Swenson, Dafang F. Wang, Michael Steffen, Dana H. Brooks, Peter M. Van Dam, and Rob S. MacLeod. A toolkit for forward/inverse problems in electrocardiography within the scirun problem solving environment. pages 267–270, 2011.
- [34] Jaume Coll-Font, Brett M Burton, Jess D Tate, Burak Erem, Darrel J Swenson, Dafang Wang, Dana H Brooks, Peter Van Dam, and Rob S Macleod. New additions to the toolkit for forward/inverse problems in electrocardiography within the scirun problem solving environment, 2014.

- [35] Adriaan van Oosterom. A comparison of electrocardiographic imaging based on two source types. *Europace : European pacing, arrhythmias, and cardiac electrophysiology : journal of the working groups on cardiac pacing, arrhythmias, and cardiac cellular electrophysiology of the European Society of Cardiology*, 16:iv120–iv128, 11 2014.
- [36] Laura R. Bear, Leo K. Cheng, Ian J. LeGrice, Gregory B. Sands, Nigel A. Lever, David J. Paterson, and Bruce H. Smaill. Forward problem of electrocardiography: Is it solved? *Circulation: Arrhythmia and Electrophysiology*, 8:677–684, 6 2015.
- [37] Charulatha Ramanathan and Yoram Rudy. Electrocardiographic imaging: II. effect of torso inhomogeneities on noninvasive reconstruction of epicardial potentials, electrograms, and isochrones. *Journal of Cardiovascular Electrophysiology*, 12:241–252, 2001.
- [38] Ruth Nicholson Klepfer, Associate Member, Christopher R Johnson, and Robert S Macleod. The effects of inhomogeneities and anisotropies on electrocardiographic fields: A 3-d finite-element study. *IEEE TRANSACTIONS ON BIOMEDICAL ENGINEERING*, 44, 1997.
- [39] Matti Stenroos and Jens Haueisen. Boundary element computations in the forward and inverse problems of electrocardiography: Comparison of collocation and galerkin weightings. *IEEE Transactions on Biomedical Engineering*, 55:2124–2133, 9 2008.
- [40] M. J.M. Cluitmans, R. L.M. Peeters, R. L. Westra, and P. G.A. Volders. Noninvasive reconstruction of cardiac electrical activity: Update on current methods, applications and challenges, 6 2015.
- [41] R.M. Gulrajani. The forward and inverse problems of electrocardiography. *IEEE Engineering in Medicine and Biology Magazine*, 17:84–101, 122, 1998.
- [42] Roger C. Barr, Maynard Ramsey, and Madison S. Spach. Relating epicardial to body surface potential distributions by means of transfer coefficients based on geometry measurements. *IEEE Transactions on Biomedical Engineering*, BME-24:1–11, 1977.
- [43] Augustus D. Waller. A demonstration on man of electromotive changes accompanying the heart's beat. *The Journal of Physiology*, 8:229–234, 10 1887.
- [44] W. Einthoven. Ein neues galvanometer. *Annalen der Physik*, 317:1059–1071, 1903.
- [45] Frank N. Wilson, Franklin D. Johnston, A.Garrard Macleod, and Paul S. Barker. Electrocardiograms that represent the potential variations of a single electrode. *American Heart Journal*, 9:447–458, 4 1934.

- [46] Gunnar Seemann, Frank B Sachse, Michael Karl, Dieter L Weiss, Vincent Heuveline, and Olaf Dössel. *Framework for Modular, Flexible and Efficient Solving the Cardiac Bidomain Equations Using PETSc*, volume 15. Springer, Berlin, Heidelberg, 2010.
- [47] Joakim Sundnes, Bjørn Fredrik Nielsen, Kent Andre Mardal, Xing Cai, Glenn Terje Lines, and Aslak Tveito. On the computational complexity of the bidomain and the monodomain models of electrophysiology. *Annals of Biomedical Engineering*, 34:1088–1097, 7 2006.
- [48] Fergus Cooper, Ruth Baker, Miguel Bernabeu, Rafel Bordas, Louise Bowler, Alfonso Bueno-Orovio, Helen Byrne, Valentina Carapella, Louie Cardone-Noott, Jonathan Cooper, Sara Dutta, Benjamin Evans, Alexander Fletcher, James Grogan, Wenxian Guo, Daniel Harvey, Maurice Hendrix, David Kay, Jochen Kursawe, Philip Maini, Beth McMillan, Gary Mirams, James Osborne, Pras Pathmanathan, Joe Pitt-Francis, Martin Robinson, Blanca Rodriguez, Raymond Spiteri, and David Gavaghan. Chaste: Cancer, heart and soft tissue environment. *Journal of Open Source Software*, 5:1848, 3 2020.
- [49] A. Quarteroni, A. Manzoni, and C. Vergara. The cardiovascular system: Mathematical modelling, numerical algorithms and clinical applications. *Acta Numerica*, 26:365–590, 5 2017.
- [50] Steven G Parker and Christopher R Johnson. Scirun: A scientific programming environment for computational steering, 1995.
- [51] M Tomita, K Hashimoto, K Takahashi, T S Shimizu, Y Matsuzaki, F Miyoshi, K Saito, S Tanida, K Yugi, J C Venter, and C A Hutchison. E-cell: software environment for whole-cell simulation. *Bioinformatics*, 15:72–84, 1 1999.
- [52] S.S. Demir. Icell: an interactive web resource for simulation-based teaching and learning in electrophysiology training. pages 3501–3504. IEEE, 2003.
- [53] José L. Puglisi and Donald M. Bers. Labheart: an interactive computer model of rabbit ventricular myocyte ion channels and ca transport. *American Journal of Physiology-Cell Physiology*, 281:C2049–C2060, 12 2001.
- [54] S.A. Blackett, D. Bullivant, C. Stevens, and P.J. Hunter. Open source software infrastructure for computational biology and visualization. pages 6079–6080. IEEE, 2005.
- [55] Olaf Dössel, Giorgio Luongo, Claudia Nagel, and Axel Loewe. Computer modeling of the heart for ecg interpretation—a review. *Hearts*, 2:350–368, 7 2021.
- [56] Aurore Lyon, Ana Mincholé, Juan Pablo Martínez, Pablo Laguna, and Blanca Rodriguez. Computational techniques for ecg analysis and interpretation in light of their contribution to medical advances, 1 2018.

- [57] Mark Potse. Scalable and accurate ecg simulation for reaction-diffusion models of the human heart. *Frontiers in Physiology*, 9, 4 2018.
- [58] Simone Pezzuto, Peter Kal'avský, Mark Potse, Frits W. Prinzen, Angelo Auricchio, and Rolf Krause. Evaluation of a rapid anisotropic model for ecg simulation. *Frontiers in Physiology*, 8, 5 2017.
- [59] David U.J. Keller, Frank M. Weber, Gunnar Seemann, and Olaf Dössel. Ranking the influence of tissue conductivities on forward-calculated ecgs. *IEEE Transactions on Biomedical Engineering*, 57:1568–1576, 2010.
- [60] Olaf Dössel, Martin W. Krueger, Frank M. Weber, Mathias Wilhelms, and Gunnar Seemann. Computational modeling of the human atrial anatomy and electrophysiology, 8 2012.
- [61] Louie Cardone-Noott, Alfonso Bueno-Orovio, Ana Mincholé, Nejib Zemzemi, and Blanca Rodriguez. Human ventricular activation sequence and the simulation of the electrocardiographic qrs complex and its variability in healthy and intraventricular block conditions. *Europace : European pacing, arrhythmias, and cardiac electrophysiology : journal of the working groups on cardiac pacing, arrhythmias, and cardiac cellular electrophysiology of the European Society of Cardiology*, 18:iv4–iv15, 12 2016.
- [62] Willi Kahlmann, Emanuel Poremba, Danila Potyagaylo, Olaf Dössel, and Axel Loewe. Modelling of patient-specific purkinje activation based on measured ecgs. *Current Directions in Biomedical Engineering*, 3:171–174, 9 2017.
- [63] Jonathan P. Cranford, Thomas J. O'Hara, Christopher T. Villongco, Omar M. Hafez, Robert C. Blake, Joseph Loscalzo, Jean Luc Fattebert, David F. Richards, Xiaohua Zhang, James N. Glosli, Andrew D. McCulloch, David E. Krummen, Felice C. Lightstone, and Sergio E. Wong. Efficient computational modeling of human ventricular activation and its electrocardiographic representation: A sensitivity study. *Cardiovascular Engineering and Technology*, 9:447–467, 9 2018.
- [64] Ana Mincholé, Ernesto Zacur, Rina Ariga, Vicente Grau, and Blanca Rodriguez. Mri-based computational torso/biventricular multiscale models to investigate the impact of anatomical variability on the ecg qrs complex. *Frontiers in Physiology*, 10, 8 2019.
- [65] Simone Pezzuto, Frits W. Prinzen, Mark Potse, Francesco Maffessanti, François Regoli, Maria Luce Caputo, Giulio Conte, Rolf Krause, and Angelo Auricchio. Reconstruction of three-dimensional biventricular activation based on the 12-lead electrocardiogram via patient-specific modelling. *Europace*, 23:640–647, 4 2021.

- [66] Joel Xue, Yao Chen, Xiaodong Han, and Weihua Gao. Electrocardiographic morphology changes with different type of repolarization dispersions. volume 43, pages 553–559, 11 2010.
- [67] David U.J. Keller, Daniel L. Weiss, Olaf Dössel, and Gunnar Seemann. Influence of i ks heterogeneities on the genesis of the t-wave: A computational evaluation. *IEEE Transactions on Biomedical Engineering*, 59:311–322, 2 2012.
- [68] Robin Moss, Eike M. Wulfers, and Gunnar Seemann. T-wave changes due to cardiac deformation are dependent on the temporal relationship between repolarization and diastolic phase. volume 2018-September. IEEE Computer Society, 9 2018.
- [69] Vincent Jacquemet. Modeling left and right atrial contributions to the ecg: A dipole-current source approach. *Computers in Biology and Medicine*, 65:192–199, 10 2015.
- [70] Mark Potse, Theo A.R. Lankveld, Stef Zeemering, Pieter C. Dagnelie, Coen D.A. Stehouwer, Ronald M. Henry, André C. Linnenbank, Nico H.L. Kuijpers, and Ulrich Schotten. P-wave complexity in normal subjects and computer models. *Journal of Electrocardiology*, 49:545–553, 7 2016.
- [71] Axel Loewe, Martin W. Krueger, Fredrik Holmqvist, Olaf Dössel, Gunnar Seemann, and Pyotr G. Platonov. Influence of the earliest right atrial activation site and its proximity to interatrial connections on p-wave morphology. *Europace : European pacing, arrhythmias, and cardiac electrophysiology : journal of the working groups on cardiac pacing, arrhythmias, and cardiac cellular electrophysiology of the European Society of Cardiology*, 18:iv35–iv43, 12 2016.
- [72] Robin Andlauer, Gunnar Seemann, Lukas Baron, Olaf Dössel, Peter Kohl, Pyotr Platonov, and Axel Loewe. Influence of left atrial size on p-wave morphology: Differential effects of dilation and hypertrophy. *Europace*, 20:III36–III44, 11 2018.
- [73] Julie J. Uv and Hermenegild Arevalo. Electrophysiological simulation of maternal-fetal ecg on a 3d maternal torso model. volume 2022-September. IEEE Computer Society, 2022.
- [74] Patricia Martinez Diaz, Jorge Sanchez, Claudia Nagel, Marta Martinez Perez, Ismael Hernandez Romero, Maraa S. Guillen, Olaf Dössel, and Axel Loewe. Personalized modeling of atrial activation and p-waves: a comparison between invasive and non-invasive cardiac mapping. volume 2022-September. IEEE Computer Society, 2022.
- [75] Cristian Barrios Espinosa, Jorge Sanchez, Olaf Dössel, and Axel Loewe. Difusion reaction eikonal alternant model: Towards fast simulations of complex cardiac arrhythmias. volume 2022-September. IEEE Computer Society, 2022.

- [76] José Alonso Solís-Lemus, Tiffany Baptiste, Rosie Barrows, Charles Sillett, Ali Gharaviri, Giulia Raffaele, Orod Razeghi, Marina Strocchi, Iain Sim, Irum Kotadia, Neil Bodagh, Daniel O'Hare, Mark O'Neill, Steven E. Williams, Caroline Roney, and Steven Niederer. Evaluation of an open-source pipeline to create patient-specific left atrial models: A reproducibility study. *Computers in Biology and Medicine*, 162:107009, 8 2023.
- [77] Karli Gillette, Matthias A. F. Gsell, Claudia Nagel, Jule Bender, Benjamin Winkler, Steven E. Williams, Markus Bär, Tobias Schäffter, Olaf Dössel, Gernot Plank, and Axel Loewe. Medalcare-xl: 16,900 healthy and pathological 12 lead ecgs obtained through electrophysiological simulations. 11 2022.
- [78] Karli Gillette, Matthias A.F. Gsell, Marina Strocchi, Thomas Grandits, Aurel Neic, Martin Manninger, Daniel Scherr, Caroline H. Roney, Anton J. Prassl, Christoph M. Augustin, Edward J. Vigmond, and Gernot Plank. A personalized real-time virtual model of whole heart electrophysiology. *Frontiers in Physiology*, 13, 9 2022.
- [79] Martin J. Bishop, Edward Vigmond, and Gernot Plank. Cardiac bidomain bath-loading effects during arrhythmias: Interaction with anatomical heterogeneity. *Biophysical Journal*, 101:2871–2881, 12 2011.
- [80] Shuang Qian, Sofia Monaci, Caroline Mendonca-Costa, Fernando Campos, Philip Gemmell, Hassan A Zaidi, Ronak Rajani, John Whitaker, Christopher A Rinaldi, and Martin J Bishop. Additional coils mitigate elevated defibrillation threshold in right-sided implantable cardioverter defibrillator generator placement: a simulation study. *Europace*, 25, 6 2023.
- [81] J. D. Bayer, R. C. Blake, G. Plank, and N. A. Trayanova. A novel rule-based algorithm for assigning myocardial fiber orientation to computational heart models. *Annals of Biomedical Engineering*, 40:2243–2254, 10 2012.
- [82] Carlos Bedregal and Maria Cecilia Rivara. Longest-edge algorithms for size-optimal refinement of triangulations. *CAD Computer Aided Design*, 46:246–251, 2014.
- [83] Aurel Neic, Matthias A.F. Gsell, Elias Karabelas, Anton J. Prassl, and Gernot Plank. Automating image-based mesh generation and manipulation tasks in cardiac modeling workflows using meshtool. *SoftwareX*, 11, 1 2020.
- [84] Marc Courtemanche, Rafael J Ramirez, and Stanley Nattel. Ionic mechanisms underlying human atrial action potential properties: insights from a mathematical model. *The American Journal of Physiology*, 1998.
- [85] K H W J Ten Tusscher, D Noble, P J Noble, A V Panfilov, Ten Tusscher, and Utrecht Univ. A model for human ventricular tissue. *Am J Physiol Heart Circ Physiol*, 286:1573–1589, 2004.

- [86] S. A. Niederer, M. Fink, D. Noble, and N. P. Smith. A meta-analysis of cardiac electrophysiology computational models. *Experimental Physiology*, 94:486–495, 2009.
- [87] Caroline Mendonca Costa, Elena Hoetzl, Bernardo Martins Rocha, Anton J Prassl, and Gernot Plank. Automatic parameterization strategy for cardiac electrophysiology simulations. *Computing in cardiology*, 40:373–376, 10 2013.
- [88] D E Roberts and A M Scher. Effect of tissue anisotropy on extracellular potential fields in canine myocardium in situ. *Circulation Research*, 50:342–351, 3 1982.
- [89] Bryan J. Caldwell, Mark L. Trew, Gregory B. Sands, Darren A. Hooks, Ian J. LeGrice, and Bruce H. Smaill. Three distinct directions of intramural activation reveal nonuniform side-to-side electrical coupling of ventricular myocytes. *Circulation: Arrhythmia and Electrophysiology*, 2:433–440, 8 2009.
- [90] A. C. Guyton and J. E. Hall. *Textbook of Medical Physiology*. Elsevier Saunders, 2006.
- [91] Ary L. Goldberger, Zachary D. Goldberger, and Alexei Shvilkin. *Goldberger's Clinical Electrocardiography*. Elsevier, 9 edition, 2018.
- [92] Thomas Williams, Colin Kelley, Christoph Bersch, Hans-Bernhard Bröker, John Campbell, Robert Cunningham, David Denholm, Gershon Elber, Roger Fearick, Carsten Grammes, Lucas Hart, Lars Hecking, Péter Juhász, Thomas Koenig, David Kotz, Ed Kubaitis, Russell Lang, Timothée Lecomte, Alexander Lehmann, Jérôme Lodewyck, Alexander Mai, Bastian Märkisch, Ethan A Merritt, Petr Mikulík, Daniel Sebald, Carsten Steger, Shigeharu Takeno, Tom Tkacik, Jos Van Der Woude, James R Van Zandt, Alex Woo, and Johannes Zellner. gnuplot 5.5 an interactive plotting program, 1986.
- [93] Michał Kania, Hervé Rix, Małgorzata Fereniec, Heriberto Zavala-Fernandez, Dariusz Janusek, Tomasz Mroczka, Günter Stix, and Roman Maniewski. The effect of precordial lead displacement on ecg morphology. *Medical and Biological Engineering and Computing*, 52:109–119, 2 2014.
- [94] Alena I. Kalyakulina, Igor I. Yusipov, Viktor A. Moskalenko, Alexander V. Nikolskiy, Konstantin A. Kosonogov, Grigory V. Osipov, Nikolai Y. Zolotykh, and Mikhail V. Ivanchenko. Ludb: A new open-access validation tool for electrocardiogram delineation algorithms. *IEEE Access*, 8:186181–186190, 2020.
- [95] Ary L. Goldberger, Luis A. N. Amaral, Leon Glass, Jeffrey M. Hausdorff, Plamen Ch. Ivanov, Roger G. Mark, Joseph E. Mietus, George B. Moody, Chung-Kang Peng, and H. Eugene Stanley. Physiobank, physiotoolkit, and physionet. *Circulation*, 101, 6 2000.

# A | Appendix

## A.1 Supplementary ECG Measurements

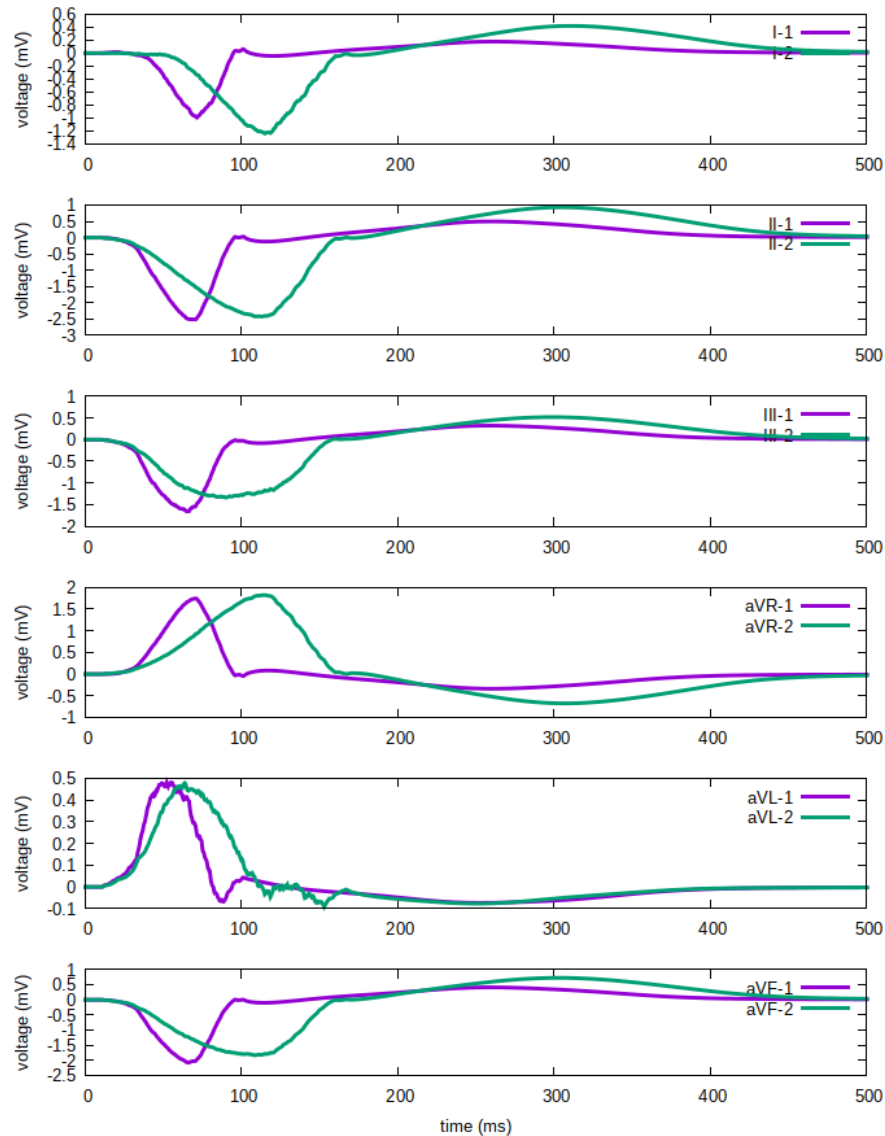


Figure A.1: Limb leads ECG measurements of different mesh structures. Purple line is for Torso 1 and green line is for Torso 2.

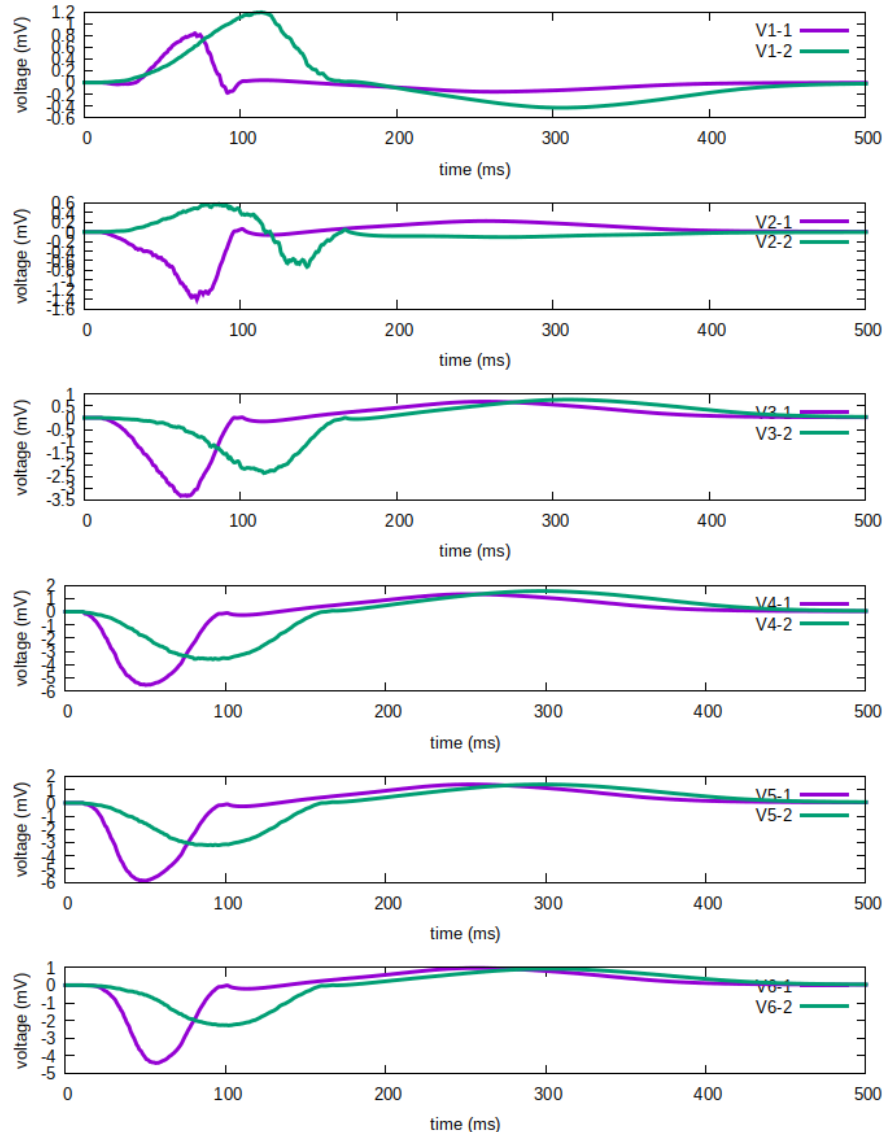


Figure A.2: Chest leads ECG measurements of different mesh structures. Purple line is for Torso 1 and green line is for Torso 2.

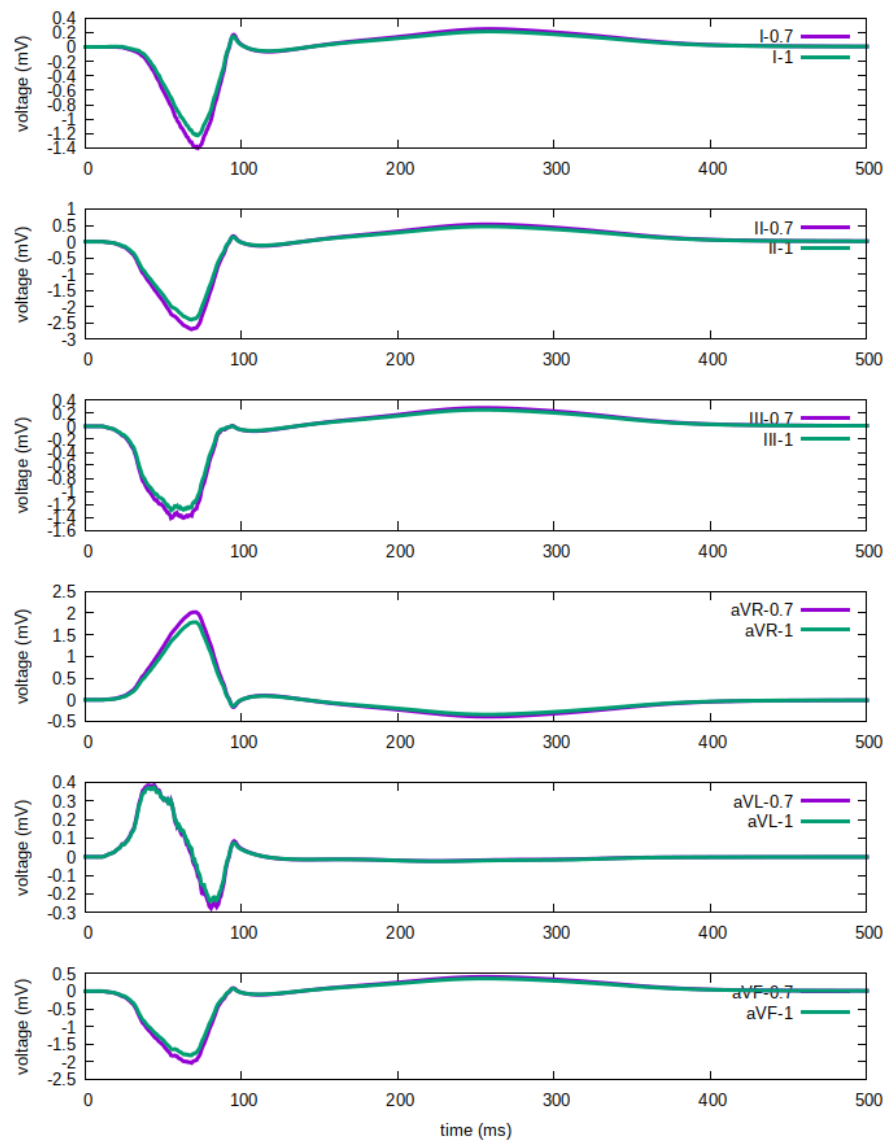


Figure A.3: Limb leads ECG measurements of meshes with different bath conductivities. Purple line is for the simulations with a bath conductivity of 0.7 and green line is for the simulations with a bath conductivity of 1.

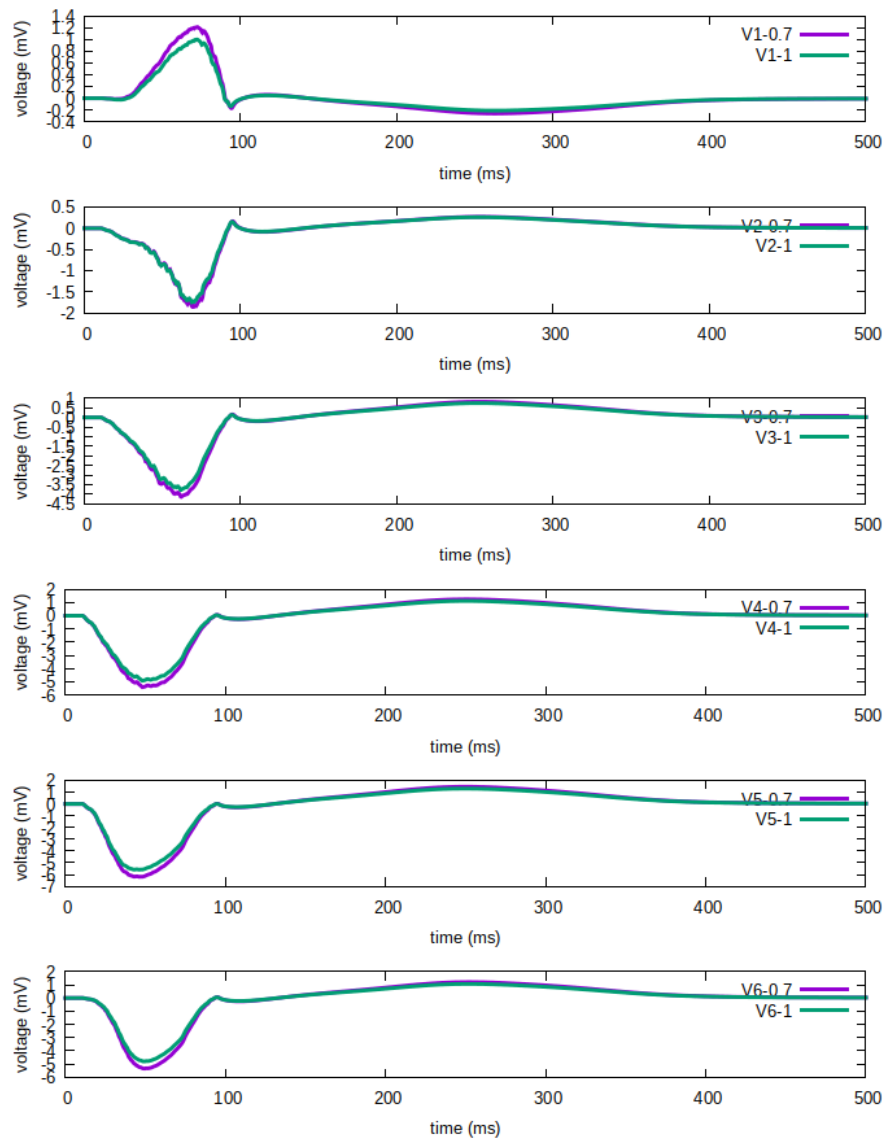


Figure A.4: Chest leads ECG measurements of meshes with different bath conductivities. Purple line is for the simulations with a bath conductivity of 0.7 and green line is for the simulations with a bath conductivity of 1.